High-Intensity Interval Training Remodels the Proteome and Acetylome of Human Skeletal Muscle

Hostrup M[1+*], Lemminger AK[1+], Stocks B[2+], Gonzalez-Franquesa A[2], Larsen JK[2], Prats Quesada J[2], Thomassen M[1], Weinert BT[3], Bangsbo J[1], & Deshmukh AS[2,4*]

[1]Section of Integrative Physiology, Department of Nutrition, Exercise and Sports, University of Copenhagen, Copenhagen, Denmark

[2]Novo Nordisk Foundation Center for Basic Metabolic Research, Faculty of Health and Medical Sciences, University of Copenhagen, Copenhagen, Denmark

[3]The Novo Nordisk Foundation Center for Biosustainability, Technical University of Denmark, Copenhagen, Denmark.

[4]The Novo Nordisk Foundation Center for Protein Research, Clinical Proteomics, Faculty of Health and Medical Sciences, University of Copenhagen, Copenhagen, Denmark.

[+]Joint first-authors

***Corresponding authors:**

Atul S Deshmukh (Lead contact)

Novo Nordisk Foundation Center for Basic Metabolic Research, Faculty of Health and Medical Sciences, University of Copenhagen, Blegdamsvej 3B, DK2200, Copenhagen, Denmark

Phone: +45 35 32 53 13; e-mail: atul.deshmukh@sund.ku.dk

Morten Hostrup

Section of Integrative Physiology, Department of Nutrition, Exercise and Sports, University of Copenhagen, 13, Universitetsparken, DK 2100, Denmark

Phone: +45 24 47 47 85; e-mail: mhostrup@nexs.ku.dk

Abstract

Exercise is an effective strategy in the prevention and treatment of metabolic diseases. Alterations in the skeletal muscle proteome, including post-translational modifications, regulate its metabolic adaptations to exercise. Here, we examined the effect of high-intensity interval training (HIIT) on the proteome and acetylome of human skeletal muscle, revealing the response of 3168 proteins and 1263 lysine acetyl-sites on 464 acetylated proteins. We identified global protein adaptations to exercise training involved in metabolism, excitation-contraction coupling, and myofibrillar calcium sensitivity. Furthermore, HIIT increased the acetylation of mitochondrial proteins, particularly those of complex V. We also highlight the regulation of exercise-responsive histone acetyl-sites. These data demonstrate the plasticity of the skeletal muscle proteome and acetylome, providing insight into the regulation of contractile, metabolic and transcriptional processes within skeletal muscle. Herein, we provide a substantial hypothesis-generating resource to stimulate further mechanistic research investigating how exercise improves metabolic health.

Impact statement

Hostrup and colleagues indentify global proteomic and acetylomic adaptations to high-intensity interval training, demonstrating apaptations to processes regulating metabolism and contraction.

Introduction

Exercise training is the most effective means to improve cardiovascular fitness and metabolic health, both being predominant determinants of life expectancy and all-cause mortality (Mandsager et al., 2018). Alterations to the proteome of skeletal muscle underpin its adaptations to exercise training, including glucose and fatty acid metabolism, insulin sensitivity, mitochondrial respiration, immune function and excitation-contraction coupling (Deshmukh et al., 2021; Egan & Zierath, 2013; Gonzalez-Franquesa et al., 2021; Holloway et al., 2009; Morten Hostrup & Bangsbo, 2017; Robinson et al., 2017; Ubaida-Mohien et al., 2019). Furthermore, proteome-wide post-translational modifications play an important role in regulating metabolism via modulating signaling, protein stability and enzyme activity (Baeza, Smallegan, & Denu, 2016; Cohen, 2000), and are sensitive to exercise stimuli (Hoffman et al., 2015; Overmyer et al., 2015; Parker, Kiens, Wojtaszewski, Richter, & James, 2020).

The application of mass-spectrometry-based proteomics has vastly expanded the catalog of post-translationally modified proteins, and in doing so has revealed novel insights into both histone and non-histone acetylation (Choudhary, Weinert, Nishida, Verdin, & Mann, 2014; Hansen et al., 2019; Narita, Weinert, & Choudhary, 2019; Svinkina et al., 2015). Nevertheless, the understanding of the acetylome in human skeletal muscle is still incomplete and remains to be studied in response to exercise training. Numerous cellular processes are regulated by protein acetylation, including transcription, metabolism, apoptosis, growth and muscle contraction among others (Narita et al., 2019). Lysine acetylation is an evolutionarily conserved post-translational modification, whereby lysine acetyltransferases catalyze the transfer of an acetyl group from acetyl-CoA to the ε-amino acid side chain of lysine and deacetylases remove acetyl groups from lysine residues. Alternatively, acetyl groups can be non-enzymatically transferred to lysine from acetyl-CoA (Hansen et al., 2019; James,

Smith, Smith, Robinson, & Murphy, 2018; Pougovkina et al., 2014; Weinert, Moustafa, Iesmantavicius, Zechner, & Choudhary, 2015). In human *vastus lateralis* muscle biopsies from male athletes, 941 acetylated proteins containing 2811 lysine acetylation sites have been identified (Lundby et al., 2012). Mitochondria were the cellular component of human skeletal muscle exhibiting the greatest proportion of acetylated proteins (Lundby et al., 2012). Furthermore, the sensitivity of the acetylome to physiological stimuli has been demonstrated in rodents in response to acute fasting and chronic caloric restriction in liver (Hebert et al., 2013; Pougovkina et al., 2014; Weinert et al., 2015) as well as acute exercise (Overmyer et al., 2015) and high-fat diet (Williams et al., 2020) in skeletal muscle (Overmyer et al., 2015).

Continual advances in mass spectrometry-based proteomic technologies and approaches are increasing the depth and coverage of proteomic analyses. Nevertheless, proteome and proteome-wide post-translational modification analyses of skeletal muscle tissue remain highly challenging due to a wide dynamic range of protein abundances (Deshmukh et al., 2015). Single-shot data-dependent acquisition (DDA) analyses are often limited in their protein identifications and are characterized by relatively poor data completeness (i.e. high number of missing values) (Tabb et al., 2010). However, the relatively recent development of data-independent acquisition (DIA) is helping to vastly reduce the proportion of missing data while simultaneously improving proteome depth in single-shot analyses of complex tissues (Ludwig et al., 2018). Nonetheless, DDA in combination with peptide-level fractionation remains a useful approach to overcome sample complexity, particularly when performing post-translational modification proteomics.

In this study, untrained men undertook five weeks of high-intensity interval training (HIIT) and *vastus lateralis* muscle biopsies were collected before and after HIIT for proteomic and lysine-acetylome

89 analyses. We investigated the adaptation to HIIT in a deep human skeletal muscle proteome and
90 undertook the first investigation of the acetylomic adaptations to exercise training within human
91 skeletal muscle. HIIT remodeled skeletal muscle favoring mitochondrial biogenesis, but induced
92 changes in protein abundance indicative of reduced calcium sensitivity. Furthermore, HIIT increased
93 acetylation, particularly of the mitochondria and enzymes of the tricarboxylic acid (TCA) cycle.
94

95 **Results and Discussion**

96 **Physiological adaptations to HIIT**

97 Eight untrained men (23–38 years of age) completed a HIIT regimen (Fig. 1A) that consisted of five
98 weeks of supervised cycling, performed as 4 – 5 × 4-min intervals at a target heart rate of >90%-max
99 interspersed by 2 mins of active recovery, undertaken three times weekly. Participants were healthy,
100 non-smokers and occasionally active, but otherwise untrained. Characteristics of the participants are
101 presented in Fig. 1B. Participants experienced a 14% and 17% improvement in maximal oxygen
102 consumption ($\dot{V}O_{2max}$) and incremental peak power output, respectively, during HIIT (Fig. 1B and C;
103 $p < 0.001$), which compares favorably to typical HIIT-induced adaptations (Wen et al., 2019). In
104 addition, participants gained an average of 1.0 ± 0.3 kg lean mass during HIIT training, without
105 changes in fat mass (Fig. 1B). The rate of fat oxidation during submaximal cycling (50-150 W)
106 increased following HIIT (Fig. 1D), while no apparent changes were observed for carbohydrate
107 oxidation (Fig. 1E).
108

109 **HIIT increases mitochondrial respiratory capacity of skeletal muscle**

110 Resting muscle biopsies were collected from the *vastus lateralis* before and three days after the final
111 training session. Mitochondrial respirometry analyses were immediately performed on the freshly
112 excised muscle samples using a substrate-uncoupler-inhibitor titration protocol (Pesta et al., 2011) on

113 a high-resolution O2K respirometer (Oroboros, Innsbruck, Austria). In line with previous findings
114 (Christensen et al., 2016; Dohlmann, Hindsø, Dela, Helge, & Larsen, 2018; Granata, Oliveira, Little,
115 Renner, & Bishop, 2016; Jacobs et al., 2013; Larsen et al., 2015; Meinild Lundby et al., 2018), HIIT
116 increased mitochondrial respiration across a range of respiratory states, increasing CI+II coupled
117 respiration by 30% ($p < 0.001$) and electron transport system capacity by 15% ($p = 0.049$) (Fig. 1F).
118 Furthermore, HIIT induced a robust increase in citrate synthase activity by 42% ($p = 0.002$) (Fig.
119 1G), a validated marker of mitochondrial volume in human skeletal muscle (Larsen et al., 2012).
120

121 **Elevated mitochondrial respiration is underpinned by increased abundance of mitochondrial**
122 **proteins following HIIT**

123 Skeletal muscle biopsy samples were prepared for liquid-chromatography tandem mass spectrometry
124 and measured using single-shot DIA (Ludwig et al., 2018) (Fig. 1H). We obtained extensive proteome
125 coverage identifying 3343 proteins (Table S1). After applying a filter of 4 valid values out of the 8
126 participants in at least one time point, 3168 proteins were quantified within skeletal muscle (Table
127 S2). Due to the nature of DIA, few missing values required imputation in each sample (Fig. S1A;
128 mean proteins quantified per sample: 2853 ± 33). Good correlation (median correlation: 0.88)
129 between biological replicates (participants at the same time point) was apparent (Fig. S1B).
130 Furthermore, the proteome contained good coverage across multiple cellular compartments (Fig.
131 S1C). Principal component analysis demonstrated inter-sample variation, however samples did
132 cluster by time point (Fig. S1D). Overall, our DIA proteome analysis displayed extensive coverage,
133 demonstrated by the quantification of low abundant proteins such as transcription factors (e.g.
134 CREB1 and TFEB) and myokines (e.g. IL18; Table S1).
135

136 HIIT regulated 126 proteins (permutation-based FDR<0.05). Of these, 102 proteins were upregulated,
137 while 24 were downregulated (Fig. 2A, Table S2). These included the upregulation of classical
138 endurance exercise training-responsive mitochondrial proteins (e.g. cytochrome c oxidase subunit 5b;
139 COX5B & NADH dehydrogenase 1 alpha subcomplex subunit 7; NDUFA7), as well as proteins
140 involved in NAD^+ metabolism (e.g. nicotinamide phosphoribosyltransferase; NAMPT), branched-
141 chain amino acid metabolism (branched-chain alpha-ketoacid dehydrogenase kinase; BCKDK) and
142 ubiquinone biosynthesis (5-demethoxyubiquinone hydroxylase; COQ7), the latter of which we have
143 recently described in exercise-trained mouse skeletal muscle (Gonzalez-Franquesa et al., 2021) (Fig.
144 2A). We also identified novel exercise-training regulated proteins, including, but not limited to,
145 glutaminyl-tRNA synthase (QARS) and rab GDP dissociation inhibitor alpha (GDI1). QARS, which
146 catalyzes the glutamate aminoacylation of tRNA and thus plays a central role in translation
147 (Deutscher, 1984), was amongst the most significantly upregulated proteins within the proteome. In
148 addition, GDI1, which inhibits insulin-stimulated glucose uptake by preventing the dissociation of
149 GDP from Rab10 (Y. Chen et al., 2009), was lowered, providing a novel potential mechanism for the
150 insulin-sensitizing effects of exercise training.
151
152 After filtering for differentially regulated proteins, enrichment analysis using Fisher's exact test
153 indicated the predominant regulation of mitochondrial proteins (e.g. GOCC: mitochondrial part and
154 mitochondrial inner membrane) (Fig. 2B, Table S3). Hierarchical clustering analysis on z-scored
155 differentially regulated proteins identified that the mitochondrial terms were enriched within the
156 upregulated proteins (Fig. 2C). Summed protein abundances also demonstrated mitochondrial
157 biogenesis (Fig. 2D), including upregulated protein content of electron transport chain complexes
158 (Fig. 2E and S2), mitochondrially-encoded proteins (Fig. 2F) and proteins containing a mitochondria-

159 targeting transit peptide (Fig. 2G). Thus, the increase in the proteome mirrors the functional increase
160 in mitochondrial respiratory capacity of skeletal muscle after HIIT (Fig. 1F).
161

162 **HIIT regulates proteins involved in skeletal muscle excitation-contraction coupling**

163 We next investigated whether HIIT influenced the fiber-type proportions of skeletal muscle. While
164 HIIT did not change skeletal muscle fiber-type composition in terms of myosin heavy chain isoforms
165 (Fig. 3A) and myosin light chain proteins (Fig. 3B), a coordinated regulation of proteins modulating
166 myosin light chain phosphorylation was identified (Fig. 3C). Abundance of myosin light chain kinase
167 2 (MYLK2) decreased concomitantly with a reduction in smoothelin-like protein 1 (SMTNL1), an
168 inhibitor of the myosin phosphatase complex (Wooldridge et al., 2008) and an increase in myosin
169 phosphatase-targeting subunit 1 (PPP1R12A), the myosin-targeting regulatory subunit of protein
170 phosphatase 1 (Alessi, MacDougall, Sola, Ikebe, & Cohen, 1992) (Fig. 3C). Reduced MYLK2
171 abundance was confirmed by immunoblotting (Fig. S3A). Furthermore, we have previously detected
172 these adaptations in slow- and fast-twitch muscle fibers following moderate-intensity continuous
173 cycling training (Deshmukh et al., 2021). Given that phosphorylation of myosin light chains promotes
174 myofibrillar calcium sensitivity (Davis et al., 2001), the reduction in both MYLK2 and SMTNL1
175 alongside an increase in PPP1R12A indicates an adaptation towards reduced myosin phosphorylation
176 and lowered calcium sensitivity following exercise training. Indeed, myofibrillar calcium sensitivity
177 decreases following high-intensity sprint training in untrained males, particularly at a low pH
178 representing physiological exercising conditions (Lynch, McKenna, & Williams, 1994). Although
179 the functional importance of such adaptations remains elusive, knockdown of Smtnl1 augments
180 exercise training-induced improvements in endurance performance, while sedentary Smtnl1$^{-/-}$ mice
181 display a fiber-type switch mimicking endurance exercise training (Wooldridge et al., 2008). While
182 we did not observe any concomitant myosin fiber-type switching (Fig. 3A), the changes observed in

183 proteins regulating myosin phosphorylation following HIIT could result in a right-shift of the Ca^{2+}-
184 force relationship, meaning that a higher myoplasmic calcium concentration would be required for a
185 given force production. This decline in myofibrillar calcium sensitivity may, however, support faster
186 off-kinetics of calcium from troponin-C to be re-sequestered in the sarcoplasmic reticulum.
187 Therefore, the changes observed in proteins regulating myosin phosphorylation following HIIT
188 provide an intriguing mechanism for a HIIT-induced reduction in calcium sensitivity and warrants
189 further attention.
190
191 Providing a further link to the altered calcium handling following HIIT (Lynch et al., 1994), we
192 identified a downregulation of L-type calcium channel subunits, otherwise known as the
193 dihydropyridine receptor (DHPR) (Figs. 3 D and E). DHPR controls the coupling of membrane
194 depolarization and sarcoplasmic reticulum Ca^{2+}-release in skeletal muscle via its interaction with
195 ryanodine receptor 1 (RYR1) (Flucher & Franzini-Armstrong, 1996). Conversely to DHPR, HIIT did
196 not influence the abundance of RYR1 (Fig. 3F) or the sarcoplasmic/endoplasmic reticulum calcium
197 ATPases 1-3 (ATP2A1-3 (SERCAs); Fig. S3B). The observation that DHPR abundance declined
198 following HIIT points to a 'slowing' of muscle fibers. Indeed, a period of training can induce rapid
199 changes in the abundance of proteins with importance for calcium handling, irrespective of changes
200 in fiber type distribution (M. Hostrup et al., 2019; M. Hostrup, Onslev, Jacobson, Wilson, & Bangsbo,
201 2018; Majerczak, Karasinski, & Zoladz, 2008; Munkvik et al., 2010; Ortenblad, Lunde, Levin,
202 Andersen, & Pedersen, 2000). Fast-twitch fibers have greater sarcoplasmic reticulum volume, faster
203 calcium release and re-uptake kinetics, and a greater content of DHPR than slow-twitch fibers (Banas,
204 Clow, Jasmin, & Renaud, 2011; Deshmukh et al., 2021; Murgia et al., 2017). Thus, the HIIT-induced
205 reduction of DHPR abundance may represent a slowing of muscle fibers independently of their
206 myosin heavy chain abundance.

207

208 **Lysine acetylomics of skeletal muscle identifies the predominant acetylation of mitochondrial**
209 **and acetyl-coA metabolic proteins**

210 Skeletal muscle biopsy samples were prepared for lysine acetylomics using a PTMscan Acetyl-Lysine
211 Motif kit (Cell Signaling Technology) (Svinkina et al., 2015) and measured via liquid-
212 chromatography tandem mass spectrometry using DDA. Due to limited sample availability from one
213 participant, lysine acetylomics was performed for 7 of the participants. We identified a total of 1990
214 acetyl-sites on 664 proteins (Table S4). While this is fewer than the 2811 acetyl-sites on 941 proteins
215 identified in the largest human skeletal muscle acetylome to date (Lundby et al., 2012), we identified
216 1073 acetyl-sites that were not identified in the analysis of Lundby et al (Fig. S4A). The difference
217 in acetyl-sites identified between the two studies likely reflects a combination of exercise-induced
218 acetylation revealing novel-acetyl sites, and the stochastic nature of data-dependent acquisition, the
219 different LC-MS/MS instruments employed, and the use of updated FASTA files. Nonetheless, we
220 substantially extend the human skeletal muscle acetylome. After applying a filter of 4 valid values
221 out of the 7 participants in at least one time point we quantified 1263 acetylated sites on 464 proteins
222 within skeletal muscle (Figs. 1G & 4A, Table S5). Six and 42 acetyl-sites were quantified exclusively
223 in the pre- and post-HIIT samples, respectively. The mean number of acetyl-sites quantified in each
224 sample was 976 (Fig. S4B). Median correlation between biological replicates (between participants
225 at the same time point) was 0.76 (Fig. S4C), indicating greater variation in the human acetylome than
226 the proteome, as would be expected (Lundby et al., 2012). The acetylome also displayed extensive
227 coverage across multiple cellular compartments (Fig. S4D), which largely reflected the abundance
228 distribution of the proteome (Fig. S1C), albeit with a slight relative increase in the mitochondrial
229 identifications. Principal component analysis identified variation in the acetylome between samples
230 (Fig. S4E). Although there was no clear separation of samples by time point, a leftward shift is

231 apparent on component 1 from pre to post samples for almost all participants (six out of seven). There
232 was considerable overlap with proteins quantified in the proteome, with 421 proteins quantified in
233 both (Fig. 4A). Of the quantified acetylated sites (1263), the majority (1232) were located on these
234 421 proteins (Fig. 4A). Single acetyl-sites were quantified on the majority of proteins, with a trend
235 for decreasing frequency with additional acetyl-sites (Fig. 4B). However, several proteins were
236 quantified with a large number of acetylation sites (e.g. ≥ 15 acetyl-sites) (Fig. 4B), examples of
237 which include the contractile proteins titin (TTN) and slow-twitch myosin beta (MYH7).
238
239 After summing the median intensities of acetyl peptides from each protein in the pre-HIIT samples,
240 we ranked the abundance of acetylated proteins within skeletal muscle (Table S6) and highlighted
241 the top 10 proteins with the highest acetyl-intensity (Fig. 4C). Histone H4 (HIST1H4A) had the
242 highest acetylation intensity, making up approximately 10% of the total acetylome intensity,
243 supporting the regulatory role of histone acetylation in modulating transcription (Sterner & Berger,
244 2000; Strahl & Allis, 2000). The majority of the remaining top acetylated proteins were metabolic
245 enzymes, including the TCA cycle proteins malate dehydrogenase (MDH2) and fumarate hydratase
246 (FH), as well as subunits of complex V (ATP5H and ATP5O) within the electron transport chain.
247 Superoxide dismutase (SOD2), a canonical acetylated enzyme involved in mitochondrial reactive
248 oxygen species handling (St Clair, Wan, Oberley, Muse, & St Clair, 1992; Z. Tao, Gao, & Liu, 2009),
249 also displayed high acetylation intensity. We further compared the protein abundance rank for these
250 high-intensity acetylated proteins within the proteome (Fig. 4D). These proteins did not appear to be
251 the highest intensity acetylated proteins simply due to their relative protein abundance. While they
252 all fell within the top 318 proteins in the proteome, they did not make up the most abundant proteins,
253 except for creatine kinase M-type (CKM), which is extremely abundant in skeletal muscle (Fig. 4D).
254 To identify systematic trends in protein acetylation, we performed a one-dimensional enrichment

255 analysis (Juergen Cox & Mann, 2012) on the summed protein acetylation intensities, which ranked
256 the proteins by acetylation intensity and identifies Gene Ontology (GO) annotations that are
257 systematically over-represented with higher intensities (positive enrichment factor) and lower
258 intensities (negative enrichment factor). This identified mitochondrial terms (e.g. GOCC:
259 mitochondrial part and mitochondrial matrix) as enriched for high acetylation intensity (Fig. 4E and
260 Table S7). In particular, proteins of carboxylic acid metabolic processes (e.g. TCA cycle) and
261 monovalent inorganic cation transport (e.g. electron transport chain complex V proteins) display
262 systematically high acetylation intensity (Fig.4E and Table S7). Furthermore, the Uniprot keyword
263 term "muscle protein" was also enriched for high acetylation intensity, a term that mainly
264 encompasses the contractile machinery of skeletal muscle (e.g. myosins).
265
266 In order to examine acetylation stoichiometry within skeletal muscle, we estimated the relative
267 stoichiometries of acetyl-sites using abundance-corrected intensities (ACI) (Table S8). ACIs were
268 calculated by dividing acetyl-peptide intensities by the intensities of their corresponding protein, with
269 ACI values correlating with stoichiometry (Hansen et al., 2019). After ranking acetyl-site ACI for the
270 pre-HIIT samples, we highlighted the top 10 acetyl-sites with the highest ACI (Fig. 4F). Trifunctional
271 enzyme subunit alpha (HADHA), FH, HIST1H4A and 3- ketoacyl-CoA thiolase (ACAA2), which
272 were identified as among the highest intensity acetylated proteins (Fig. 4C), all contain high
273 stoichiometry acetyl-sites (Fig. 4F). However, nicotinamide nucleotide transhydrogenase (NNT) K70
274 had the highest ACI within skeletal muscle (Fig. 4F). NNT is an inner mitochondrial membrane
275 protein, which uses the proton motive force to maintain high levels of NADPH (Hoek & Rydström,
276 1988) and in doing so can regulate metabolism (Freeman, Hugill, Dear, Ashcroft, & Cox, 2006; Ho,
277 Lin, Lin, Wu, & Cheng, 2017). NNT is also highly acetylated in cardiac muscle (Foster et al., 2013),
278 although the effect of acetylation on NNT activity remains to be determined. Nonetheless, NNT can

279 regulate acetylation via NADPH-mediated regulation of histone deacetylase 1 (HDAC1) activity (Ho
280 et al., 2017), thus acetylation of NNT may represent a feedback mechanism controlling cellular
281 acetylation and metabolism.
282
283 To identify systematic trends in acetyl-site stoichiometry, we performed a one-dimensional
284 enrichment analysis (Juergen Cox & Mann, 2012) on acetyl-site ACI using the leading protein ID for
285 relative enrichment (Tyanova et al., 2016). We identified the mitochondria (e.g. GOCC:
286 mitochondrial part and mitochondrial inner membrane) and carboxylic acid catabolic processes to be
287 enriched within higher stoichiometry acetylated proteins (Figs. 4G, 4H & Table S9). This extends
288 previous analyses by not only showing that mitochondrial proteins make up the majority of acetylated
289 proteins in skeletal muscle (Lundby et al., 2012), but also by identifying mitochondrial proteins as
290 having relatively high stoichiometry acetyl-sites – an observation that is consistent with analyses in
291 HeLa cells, rodent liver and yeast (Hansen et al., 2019; Weinert et al., 2014; Weinert et al., 2015).
292 Enriched for proteins with low stoichiometry acetyl-sites were proteins involved in contraction (e.g.
293 GOCC: contractile fiber part; Figs. 4G, 4H & Table S9), including the Uniprot keyword term "muscle
294 protein" (Fig. 4G), which, conversely, was enriched for high protein acetylation intensity (Fig. 4E).
295 Myosin displayed the greatest enrichment for low acetylation stoichiometry (Fig. 4G). Thus, despite
296 contractile proteins displaying high protein acetylation intensity and making up a substantial number
297 of known acetylated proteins within skeletal muscle (Lundby et al., 2012), they contain acetylation
298 sites of relatively low stoichiometry. The high acetylation intensity of these proteins is therefore likely
299 due to high protein abundance and a large number of acetylation sites per protein. Proteins annotated
300 to the cytosol and plasma membrane also displayed low acetyl-site ACI (Fig. 4G). This highlights
301 differences in the inter-organelle acetylation levels of skeletal muscle and can likely be explained by

302 subcellular compartmentalization of acetyl-CoA (Pietrocola, Galluzzi, Bravo-San Pedro, Madeo, &
303 Kroemer, 2015).
304
305 **HIIT induces acetylation of mitochondrial and TCA cycle proteins**
306 HIIT increased the mean number of acetyl-sites quantified per sample by over 100 sites (Pre: 915 ±
307 44, Post: 1037 ± 51; $p = 0.015$; Fig. S4B). Using a stringent statistical approach of permutation-based
308 FDR corrected paired t-tests, we identified 20 upregulated acetyl-sites and 1 downregulated site (FDR
309 < 0.05; Fig. 5A). In addition, by applying a validated, albeit less stringent, significance score (Π-
310 value), which combines the statistical significance (p-value) with the fold change (Xiao et al., 2014),
311 we extended this to identify 257 upregulated and 26 downregulated acetyl-sites following HIIT ($\Pi <$
312 0.05; Fig. 5A and Table S5). In general, there was a trend for increased acetylation following HIIT
313 (Fig. 4A), which could not be explained by changes in protein content as the fold changes in
314 acetylation generally exceeded those of protein abundance (Fig. 5B). Therefore, we did not normalize
315 the acetylome data to protein abundance. The increase in protein acetylation was subsequently
316 validated via immunoblotting (Fig S4F). Within the increased sites, acetyl-sites on metabolic
317 enzymes isocitrate dehydrogenase (IDH2), pyruvate dehydrogenase E1 component subunit alpha
318 (PDH1A), succinate CoA ligase subunit alpha (SUCLG1) and ATP synthase coupling factor 6
319 (ATP5J) were apparent (Fig. 5A), while hyperacetylation of SOD2 occurred at K68, 75, 122 and 130
320 in response to HIIT (Fig. 5A). Included within the downregulated sites were acetyl-sites on annexin
321 A6 (ANXA6), laminin (LMNA) and p38 mitogen-activated protein kinase γ (MAPK12) (Fig. 5A).
322 Interestingly, Histone H1.5 (HIST1H1B) K48 showed increased acetylation, despite significantly
323 reduced protein abundance (Fig. 5B).
324

325 A Fisher's exact test of HIIT-regulated acetyl-sites (Π < 0.05), using leading protein ID for relative
326 enrichment, indicated the predominant regulation of the TCA cycle pathway, mitochondrial proteins
327 (e.g. GOCC: mitochondrial part and mitochondrial inner membrane) and, in particular, electron
328 transport chain complex V proteins (GOCC: mitochondrial proton-transporting ATP synthase
329 complex) (Fig. 5C, Table S10). These GO terms were strikingly similar to the terms enriched for high
330 acetylation intensity and stoichiometry in the pre-HIIT samples (Figs. 4E and G), indicating that
331 proteins that are highly acetylated in the basal state are most susceptible to increased acetylation
332 following HIIT. To further explore the regulation of HIIT-induced acetylation in skeletal muscle, we
333 looked for consensus sequences around the acetylated lysine residues using iceLogo (Colaert,
334 Helsens, Martens, Vandekerckhove, & Gevaert, 2009). We identified a sequence with a
335 predominance of proximal cysteine residues as well as an aspartic acid residue in the +1 position (Fig.
336 5D). The aspartic acid at +1 is a feature of mitochondrial acetylated proteins (Lundby et al., 2012)
337 and its enrichment is likely due to the over-representation of mitochondrial proteins in the upregulated
338 acetyl-sites (Fig. 5C). Proximal cysteine residues are associated with promoting non-enzymatic lysine
339 acetylation (Hansen et al., 2019; James et al., 2018) via initial cysteine acetylation followed by
340 transfer of the acetyl group to lysine (James et al., 2018). Indeed, non-enzymatic acetylation increases
341 alongside elevated fatty acid oxidation (Pougovkina et al., 2014), as is apparent in skeletal muscle
342 mitochondria after HIIT (Figs. 1E). This likely occurs through changes in acetyl-CoA concentration
343 and/or increased acetyl-CoA flux (Pougovkina et al., 2014). Although acetyl-CoA content within
344 resting skeletal muscle does not change in response to exercise training (Putman et al., 1998), acetyl-
345 CoA levels and TCA cycle flux increase during exercise (Constantin-Teodosiu, Carlin, Cederblad,
346 Harrist, & Hultman, 1991; Gibala, MacLean, Graham, & Saltin, 1998; Howlett et al., 1998; Putman
347 et al., 1998), which may result in an accumulation of lysine acetylation during repeated bouts of
348 exercise. Conversely, acute exercise decreases skeletal muscle acetylation in exercising rats

349 (Overmyer et al., 2015), but whether this is the case for humans remains to be determined.
350 Nonetheless, we identify a robust increase in skeletal muscle acetylation, predominantly of
351 mitochondrial proteins, following five weeks of HIIT in humans.
352
353 Because HIIT altered the skeletal muscle acetylome, we examined proteins regulating acetylation in
354 skeletal muscle. A subset of sirtuins (SIRT2, SIRT3, and SIRT5), a family of protein deacetylases,
355 were quantified in the proteome. SIRT3, a mitochondrial-localized deacetylase, displayed a small but
356 non-significant trend for increased abundance following exercise training (Table S2). To further
357 investigate this, we immunoblotted for SIRT1, SIRT3, SIRT5 and SIRT6. Of the cystosolic and
358 nuclear-localized SIRTs, the abundance of SIRT1 did not change, while SIRT6 increased by 27%.
359 The mitochondrial-localized SIRT3 and SIRT5 increased in abundance by 61% and 32%,
360 respectively, following HIIT (Fig. 5E). Thus, mitochondrial acetylation increased concomitantly with
361 an increase in the abundance of mitochondrial sirtuins (Figs. 5B and 5E). Conversely, the protein
362 abundance of the mitochondrial acetyltransferase general control of amino acid synthesis 5 like-1
363 (GCN5L1) was unchanged by exercise training (Fig 5E). SIRT3 appears to play a major role in
364 suppressing non-enzymatic mitochondrial acetylation (Weinert et al., 2015). Therefore, the elevated
365 mitochondrial deacetylase abundance following exercise training might be interpreted as a
366 mechanism to suppress excess acetylation, either to preserve the activity of mitochondrial enzymes
367 (Hirschey et al., 2010; R. Tao et al., 2010; Vassilopoulos et al., 2014) or to scavenge acetyl groups
368 for reintegration into acetyl-CoA and energy production.
369
370 Given the enrichment of mitochondrial terms and particularly of complex V proteins in the HIIT-
371 regulated acetylated proteins, we filtered for proteins annotated to the different complexes of the
372 electron transport chain using the HUGO database (Braschi et al., 2019) and highlighted the

373 regulation of each acetyl-site on these proteins alongside the changes in protein abundance (Fig. 6A).
374 While proteins of complexes I, II, III and IV showed a mixed acetylation response to exercise training,
375 almost every quantified complex V protein had at least one acetyl-site that increased following HIIT
376 (Fig. 6A). In fact, ATPase inhibitor (ATPIF1), one of the two complex V proteins that do not show
377 elevated acetylation, is a negative regulator of complex V and is unlikely to be constitutively bound
378 to the ATP synthase complex (Campanella et al., 2008). Why complex V displays elevated
379 acetylation levels both in the basal (Fig. 4E) and exercise trained states is unclear (Figs. 5C and 6A).
380 However, as a large proportion of ATP synthase extends into the mitochondrial matrix, many subunits
381 are likely to be more exposed to acetyl-CoA than other membrane-embedded electron transport chain
382 complexes. In support, we detected acetylation on all of the subunits of complex V that reside or
383 extend into the mitochondrial matrix (ATP5A1, ATP5B, ATP5C1, ATP5D, ATP5E, ATP5F1,
384 ATP5H, ATP5J and ATP5O), while we only detect acetylation on two of the membrane-embedded
385 subunits (ATP5L and MT-ATP8), despite detecting a further four membrane-embedded subunits in
386 the proteome (ATP5I, ATP5J2, MT-ATP6 and USMG5). Indeed, the majority of acetylated proteins
387 quantified on each electron transport chain complex (CI-CV) are exposed to either the mitochondrial
388 matrix or the intermembrane space. Similarly, TCA cycle enzymes, which are localized to the
389 mitochondrial matrix, displayed high acetylation intensity and stoichiometry in the basal state and
390 HIIT augmented levels of acetylation at every stage of the cycle (Fig. 6B), again likely due to their
391 proximity to acetyl-CoA. Conversely, cytosolic proteins regulating skeletal muscle contraction
392 showed fewer upregulated acetyl-sites with a number of downregulated sites following HIIT (Fig.
393 6C). Thus, proteins in close proximity to acetyl-CoA appear to be more susceptible to acetylation.
394
395 Despite widespread HIIT-induced acetylation of mitochondrial proteins, these data should be
396 considered in the context of acetylation stoichiometry, which is generally low (Weinert et al., 2015).

397 Median acetylation stoichiometry in rodent liver has been calculated at only 0.05%, which increases
398 slightly to 0.11% for mitochondrial proteins (Weinert et al., 2015). Although acetylation is tissue-
399 dependent (Lundby et al., 2012), skeletal muscle levels are unlikely to be vastly different. The median
400 $\log_2$-fold change for mitochondrial acetyl-sites following HIIT was 0.9 (the corresponding value in
401 the proteome was 0.3), indicating that median post-HIIT stoichiometry would have remained at less
402 than 1%. Thus, the levels of HIIT-induced changes in acetylation may not be large enough to
403 influence gross activity on most metabolic enzymes. Nonetheless, physiological acetylation may be
404 high enough to be regulatory on some proteins. For example, acetylation of mitochondrial malate
405 dehydrogenase (MDH2) negatively correlates with its enzyme activity (Overmyer et al., 2015).
406 Another such enzyme could be pyruvate dehydrogenase (PDH), whose E1 component subunit alpha
407 (PDHA1) is within the top 25 most acetylated proteins (Table S6), whilst PDHA1 Lys 336 was within
408 the top 5 most upregulated acetyl-sites with exercise training (Fig. 5A). Increased acetylation of
409 PDHA1 occurs alongside suppressed enzyme activity in SIRT3 knockout mice (Jing et al., 2013). By
410 catalyzing the reaction between pyruvate and acetyl-CoA, PDH provides the link between glycolysis
411 and the tricarboxylic acid cycle (Constantin-Teodosiu, Constantin, Stephens, Laithwaite, &
412 Greenhaff, 2012). Thus, exercise-induced hyperacetylation of PDH could play a role in the metabolic
413 switch towards elevated fat oxidation following exercise training. Furthermore, mitochondrial
414 hyperacetylation increases fatty acid-supported respiration (Williams et al., 2020). These data are
415 consistent with the concomitant increase in acetylation (Fig. 5A) and mitochondrial respiratory
416 capacity and fat oxidation (Fig. 1F) following HIIT, suggesting that hyperacetylation of
417 mitochondrial proteins following exercise training may support the bioenergetic adaptations to
418 exercise.
419
420 **HIIT increases histone acetylation**

421 Aside from metabolic enzymes and contractile proteins, histones are regulated by acetylation (Sterner
422 & Berger, 2000; Strahl & Allis, 2000) and may represent a more specifically regulated pool of
423 proteins, owing to the nuclear localization of acetyltransferases (Hendzel, Sun, Chen, Rattner, &
424 Davie, 1994). Increases in certain acetylated histone residues are well characterized to augment
425 transcription, with exercise known to acutely regulate H3 acetylation (e.g. H3 K4, H3 K9/14 & H3
426 K36) (Joseph, Ayeleso, & Mukwevho, 2017; Lochmann, Thomas, Bennett, & Taylor, 2015; McGee,
427 Fairlie, Garnham, & Hargreaves, 2009; Smith, Kohn, Chetty, & Ojuka, 2008). Here we identified 18
428 distinct acetylated peptides from histones, with acetylated peptides from H1.5 (HIST1H1B K48),
429 H2B type 2F (HIST2H2BF K16/20) and H3.3 (H3F3B K23) being elevated following HIIT (Figs.
430 7A-D). H1.5 K48 was exclusively quantified in post-HIIT samples, however, it was only quantified
431 in 4 out of 7 of the post-HIIT samples, which is our minimum cut-off for valid values. The regulatory
432 roles of these HIIT-regulated histone acetyl-sites are unknown. However, acetylation of the N-
433 terminal of H2B, including K16 & K20, has been linked to transcriptional activation (H. Chen et al.,
434 2014; Parra, Kerr, Fahy, Pouchnik, & Wyrick, 2006), including the expression of NAD-metabolic
435 genes in yeast (Parra et al., 2006). The role of H3 K23 is also obscure, however, its acetylation
436 contributes to the development of cancer through the recruitment of the transcription factor
437 transcription intermediary factor 1-alpha (TRIM24) and the nuclear receptor estrogen receptor alpha
438 (ERS1) (Lv et al., 2017; Tsai et al., 2010), augmenting expression of phosphatidylinositol 4,5-
439 biphosphate 3-kinase catalytic subunit alpha (PIK3CA), a subunit of phosphoionositide-3-kinase
440 (PI3K), and phosphorylation of protein kinase B (AKT1) (Lv et al., 2017). Indeed, TRIM24 promotes
441 the abundance of glycolytic and TCA cycle genes in transforming human mammary epithelial cells
442 (Pathiraja et al., 2015), while ERS1 regulates mitochondrial biogenesis in skeletal muscle (Ribas et
443 al., 2016). Whether H3 K23 regulates TRIM24, ERS1, PI3K, and AKT1 activity and influences
444 metabolism in skeletal muscle remains unclear. Further studies are warranted to understand the

transcriptional and metabolic implications of exercise training-induced acetylation on these histone sites.

To investigate the potential regulatory role of the nuclear-localized histone acetyltransferase p300 (EP300) in the acetylation of these exercise-responsive histone sites, we knocked down EP300 in C2C12 myotubes and assessed the acetylation of H2B K20 and H3 K23 via immunoblotting. Knockdown of EP300 reduced acetylation of H2B K20 by 48%, whilst acetylation of H3 K23 was unaffected (Fig 7E). These analyses identify EP300 as an acetyltransferase responsible for the acetylation of H2B K20 in skeletal muscle.

Conclusion

Here, we leveraged advances in DIA mass spectrometry to produce a deep human skeletal muscle proteome and applied this approach to ascertain exercise training adaptations. Furthermore, we provide the first investigation of the human acetylome in response to exercise training. In the proteome, we highlight known and novel exercise-responsive proteins, including a potential mechanism to explain altered skeletal muscle calcium sensitivity following HIIT. In the acetylome, we describe the predominant acetylation of mitochondrial proteins after HIIT, particularly of TCA cycle proteins and subunits of electron transport chain complex V, as well as highlighting the regulation of novel exercise-responsive histone acetyl-sites. Altogether, we provide a substantial hypothesis-generating resource, identifying novel exercise-regulated proteins and acetyl-sites with the aim of stimulating further mechanistic research investigating how exercise improves metabolic health.

Materials and Methods

469 *Participants*

470 Participants were enrolled by AKL and MH between August and September 2017. Eight men were
471 assessed for eligibility. All eight men were eligible and gave their informed consent after receiving
472 written and oral information about the study and potential risks associated with the experimental
473 procedures (Fig. S5). Inclusion criteria were healthy males, 18-40 years old, $\dot{V}O_{2max}$ between 45-55
474 $mL \cdot min^{-1} \cdot kg^{-1}$ or 3000-4000 $mL \cdot min^{-1}$ and BMI between 19-26 $kg \cdot m^{-2}$. Exclusion criteria were
475 abnormal electrocardiogram, chronic disease, ongoing medical treatment, and smoking. Subject
476 characteristics are presented in Table 1. The study was approved by the National Committee on
477 Health Research Ethics (H-17004045) and registered at clinicaltrials.gov (NCT03270475). The study
478 complied with the Declaration of Helsinki (2013).

479

480 *Study outcomes*

481 The pre-determined primary outcome was the change from baseline in the skeletal muscle proteome.
482 Secondary outcomes were changes from baseline in the skeletal muscle acetylome, skeletal muscle
483 mitochondrial respiration and whole-body maximal oxygen consumption ($\dot{V}O_{2max}$).

484

485 *Experimental trials*

486 The study consisted of two experimental days separated by five weeks of high-intensity interval
487 training (HIIT). At each experimental day, body composition was measured by dual-energy X-ray
488 absorptiometry (DXA) scans (Lunar iDXA, GE Healthcare, GE Medical systems, Belgium). Then,
489 subjects rested in a supine position for 15 min and two 4 mm incisions separated by 2 cm were made
490 in the above the *vastus lateralis* muscle under local anaesthesia (Xylocaine 20 $mg \cdot mL^{-1}$ without
491 epinephrine, AstraZeneca, London, UK) and a muscle biopsy was taken from each incision using a
492 Bergström needle with suction. Afterwards, $\dot{V}O_{2max}$ was determined by indirect calorimetry using a

493 breath-by-breath gas analyser (Oxycon Pro, CareFusion, San Diego, USA) during an incremental test
494 on a bike ergometer (Monark LC4, Monark Exercise, Vansbro, Sweden). The incremental test
495 consisted of 5 min rest followed by 4 min stages at 50, 100, 150 W, after which the resistance was
496 increased in increments of 30 $W \cdot min^{-1}$ until exhaustion. Time to exhaustion was used to calculate
497 incremental peak power output (iPPO) accounting for time spent at the last increment. Subjects
498 completed the experimental protocol the same time of day before and after the intervention and were
499 instructed to eat a small meal with 500 mL water two hours before arriving at the laboratory. In
500 addition, subjects abstained from alcohol, caffeine, and physical activity for 48 h before each
501 experimental day and were instructed to maintain their activity level and diet during the study. The
502 experimental days were performed three days before and after the first and last training, respectively.
503 All experimental trials were performed at the Department of Nutrition, Exercise and Sports,
504 University of Copenhagen. Experimental trials were completed in October 2017.
505
506 *Body composition*
507 At each experimental day, two scans were performed to reduce scan-to-scan variation (Nana, Slater,
508 Hopkins, & Burke, 2012). Before the first scanning, subjects rested in a supine position for 10 min to
509 allow fluid distribution reducing intra-scan variation (Berg, Tedner, & Tesch, 1993; Cerniglia,
510 Delmonico, Lindle, Hurley, & Rogers, 2007). Whole-body and leg composition were calculated using
511 software (enCORE Forma v. 15, GE Healthcare Lunar, Buckinghamshire, UK).
512
513 *Substrate utilization*
514 Gas exchange measurements during rest and submaximal exercise were used to calculate fat and
515 glucose oxidative as previously described (Jeukendrup & Wallis, 2005) and corrected for protein

516 oxidation (Lee, Day, Greenfield, & Ho, 2013). Fat oxidation and carbohydrate oxidation were
517 calculated as:

518 $$Fat\ Oxidation\left(\frac{mg}{min}\right) = \left(1.695 \cdot \dot{V}O_2 - 1.701 \cdot \dot{V}CO_2\right) - \frac{1.92 \cdot 0.14 \cdot BM}{1440}$$

519 $$Carbohydrate\ Oxidation\left(\frac{mg}{min}\right) = \left(4.344 \cdot \dot{V}CO_2 - 3.061 \cdot \dot{V}O_2\right) - \frac{2.87 \cdot 0.14 \cdot BM}{1440}$$

520 where $\dot{V}O_2$ and $\dot{V}CO_2$ are in L·min^{-1} and *BM (Body mass)* is in kg.

521

522 *Muscle biopsies*

523 Immediately after collection, muscle biopsies were rinsed in ice-cold saline. A small piece (~15 mg)
524 of the muscle was transferred into ice-cold preservation solution (BIOPS) for analysis of
525 mitochondrial respiratory capacity. The remaining muscle tissue was snap-frozen in liquid nitrogen
526 and stored at –80°C. The frozen muscle samples were freeze-dried for 48 h and dissected free from
527 connective tissues, fat and blood under a microscope in a humidity-controlled room (~25% humidity)
528 before storage at –80°C for later analyses.

529

530 *High intensity interval training*

531 Subjects underwent a five-week high-intensity interval training intervention consisting of three
532 weekly training sessions with 4-5 × 4 min intervals interspersed by two min active recovery on indoor
533 spinning bikes. The training volume increased from four intervals during the first two weeks to five
534 intervals during the last three weeks. During each interval, subjects were instructed to reach >90% of
535 maximal heart rate (HR_{max}). All training sessions were supervised and subjects received verbal
536 encouragement during all intervals. The mean HR_{max} during intervals was 96 ± 1% of HR_{max}.

537

538 *Mitochondrial profiling*

539 Mitochondrial respiratory capacity was determined in duplicate by high-resolution respirometry
540 (Oxygraph-2k, Oroboros Instruments, Innsbruck, Austria) at 37°C using 1-3 mg wet weight muscle
541 fibers per chamber in MiR06. Oxygen concentrations were kept between 200 and 450 µM throughout
542 the experiment. The muscle sample in BIOPS was prepared for high-resolution respirometry as
543 previously described (Pesta & Gnaiger, 2012). In short, muscle fibers were dissected free from
544 connective tissue and fat followed by permeabilization in BIOPS with saponin and washed in
545 mitochondrial respiration buffer (MiR06). A substrate-uncoupler-inhibitor titration protocol was used
546 to assess different respiratory states as previously described (Pesta et al., 2011). Leak respiration (L_N)
547 in the absence of adenylates was induced by the addition of malate (2 mM) and octanoylcarnitine (0.2
548 mM). Fatty acid oxidation (FAO) was determined after titration of ADP (2.5 mM). Submaximal CI
549 and CI+II-linked respiration (CI_D & P_D) was measured in the presence of glutamate (10 mM) and
550 succinate (10 mM), respectively. Oxidative phosphorylation capacity (P) was assessed after another
551 titration of ADP (2.5 mM). The mitochondrial outer membrane integrity was then tested with the
552 addition of cytochrome C (10 µM). The average change in oxygen flux was 3.8% (range: 0.2-9.4%).
553 Respiratory electron transfer-pathway capacity (E) was measured during step-wise (0.5 µM) titration
554 of carbonyl cyanide p-trifluoro-methoxyphenyl hydrazine (FCCP). Succinate-supported electron
555 transfer-pathway capacity (E_{CII}) was assessed by the addition of rotenone (0.5 µM). Residual oxygen
556 consumption was determined after the addition of malonic acid (5 mM), myxothaizol (0.5 µM) and
557 antimycin A (2.5 µM) and subtracted from each respiratory state.
558
559 Maximal enzyme activity of citrate synthase was determined from muscle homogenate using
560 fluorometry (Fluoroscan Ascent, Thermo Fisher Scientific, Waltham, USA) at 25°C as previously
561 described (Lowry, 2012).
562

563 *Proteomic sample preparation*

564 Human skeletal muscles were lysed in a buffer consisting of 1% Sodium Deoxycholate (SDC), 10
565 mM Tris (2-carboxyethyl) phosphine (TCEP), 40 mM Chloroacetamide (CAA) and 100 mM of Tris
566 (pH 8.5). The muscles were homogenized with an Ultra Turrax homogenizer (IKA). Lysates were
567 boiled at 95°C for 10 min and sonicated using a tip sonicator. Lysates were then centrifuged at 16000g
568 for 10 min. Proteins were digested using the endoproteinases LysC and trypsin (1:100 w/w) at 37°C
569 overnight with shaking. Digested peptides were acidified using 1% Trifluoroacetic acid (TFA) and
570 precipitated SDC was removed by centrifugation. Peptides were purified using Sep-pak C18
571 cartridges (Waters) and were eluted in 50% acetonitrile. 20 µg of peptides were saved for total
572 proteome analysis while 3 mg peptides were saved for enrichment of acetylated peptides.

573

574 *Acetylated peptide enrichment*

575 The acetyl peptide enrichment was performed on 3 mg of digested peptides using PTMscan Acetyl-
576 Lysine Motif kit (Cell Signaling #13416). The peptides were mixed with 100 µL of 10x IP buffer
577 (500 mM MOPS, pH 7.2, 100 mM Na-phosphate, 500 mM NaCl, 5% NP-40). The acetonitrile was
578 removed and the volume was reduced to ~1mL by vacuum centrifugation. The final volume was
579 adjusted with water to a concentration of 3 $mg \cdot mL^{-1}$. The peptides were clarified by centrifugation at
580 20000g for 5 min. 20 µL of anti-acetylated lysine antibody was washed 3 times in 1 mL IP buffer and
581 then mixed with the peptides. Peptides were enriched overnight at 4°C, washed 3 times in 1 mL ice-
582 cold (4°C) IP buffer, 4 times in 1 mL ice-cold IP buffer without NP-40, and once in 1 mL water. All
583 wash buffer was removed via aspiration. Acetylated peptides were eluted with 100 µL 0.15% TFA.
584 The elution procedure was repeated three times. The eluted peptides were de-salted on C18 stage-tips
585 (Rappsilber, Mann, & Ishihama, 2007), vacuum concentrated and resuspended in buffer A* (5%
586 acetonitrile, 0.1% trifluoroacetic acid).

587

588 *High pH reversed-phase fractionation*

589 To generate a deep proteome library for data-independent acquisition (DIA), 50 µg of peptide was
590 pooled from pre- and post-HIIT samples, separately, and fractionated using high pH reversed-phase
591 chromatography (Kulak, Geyer, & Mann, 2017). 24 fractions (per pool) were automatically
592 concatenated using a rotor valve shift of 90 s. Approximately 0.3 µg of each fraction were subjected
593 to LC-MS/MS measurements via data-dependent acquisition (DDA). To obtain comprehensive
594 coverage of the acetylome, acetylated peptides from each sample were fractionated into 8 fractions
595 using a rotor valve shift of 90 s. For the first subject (both pre and post samples) all 8 fractions were
596 analysed separately. After observing lower than expected peptide intensities for the first subject, the
597 neighboring two factions were pooled together for each of the remaining samples (total four
598 fractions/subject/timepoint) before LC-MS analysis.

599

600 *Mass spectrometry*

601 Peptides were measured using LC-MS instrumentation consisting of an Easy nanoflow HPLC system
602 (Thermo Fisher Scientific, Bremen, Germany) coupled via a nanoelectrospray ion source (Thermo
603 Fischer Scientific, Bremen, Germany) to a Q Exactive HF-X mass spectrometer. Purified peptides
604 were separated on a 50 cm C18 column (inner diameter 75 µm, 1.8 µm beads, Dr. Maisch GmbH,
605 Germany). Peptides were loaded onto the column with buffer A (0.5% formic acid) and eluted with
606 a 100 min linear gradient increasing from 2-40% buffer B (80% acetonitrile, 0.5% formic acid). After
607 the gradient, the column was washed with 90% buffer B and re-equilibrated with buffer A. Peptides
608 were measured in singleton.

609

610 For the deep proteome library generation, mass spectra were acquired from each fraction via DDA
611 with automatic switching between MS and MS/MS using a top 15 method. MS spectra were acquired
612 in the Orbitrap analyzer with a mass range of 300-1750 m/z and 60,000 resolutions at m/z 200 with
613 a target of 3 x 10^6 ions and a maximum injection time of 25 ms. HCD peptide fragments acquired at
614 27 normalized collision energy were analyzed at 15000 resolution in the Orbitrap analyzer with a
615 target of 1 x 105 ions and a maximum injection time of 28 ms. The mass spectra for the acetylome
616 experiments were also acquired from each fraction via DDA with a similar MS method used for deep
617 proteome library generation, except the maximum injection time for the fragment ion spectra was set
618 to 250 ms. A DIA MS method was used for the total proteome measurements in which one full scan
619 (300 to 1650 *m/z*, resolution = 60,000 at 200 *m/z*) at a target of 3 x 10^6 ions was first performed,
620 followed by 32 windows with a resolution of 30000 where precursor ions were fragmented with
621 higher-energy collisional dissociation (stepped collision energy 25%, 27.5%, 30%) and analyzed with
622 an AGC target of 3 x 10^6 ions and maximum injection time at 54 ms in profile mode using positive
623 polarity.
624
625 *Data processing*
626 Raw MS files from the experiments measured in DDA mode (muscle proteome library & acetylome),
627 were processed using MaxQuant (J. Cox & Mann, 2008). MS/MS spectra were searched by the
628 Andromeda search engine (integrated into MaxQuant) against the decoy UniProt-human database
629 (downloaded in December 2017) with forward and reverse sequences. In the main Andromeda search
630 precursor, mass and fragment mass were matched with an initial mass tolerance of 6 ppm and 20
631 ppm, respectively. The search included variable modifications of methionine oxidation and N-
632 terminal acetylation and fixed modification of carbamidomethyl cysteine. For the raw files from the
633 acetylome experiments, acetylated lysine was also added as a variable modification. Acetylated

634 peptides were filtered for a minimum Andromeda score of 40, as per the default settings for modified
635 peptides. The false discovery rate (FDR) was estimated for peptides and proteins individually using
636 a target-decoy approach allowing a maximum of 1% false identifications from a revered sequence
637 database. Raw files acquired in the DIA mode (total proteome) were processed using Biognosys
638 Spectronaut software version 13 (Bruderer et al., 2015). A single peptide library was generated in
639 Spectronaut using the combined MaxQuant search results for the DDA runs from both of the
640 fractionated muscle samples. The experimental DIA runs were then analyzed in Spectronaut using
641 default settings.
642
643 *Bioinformatics*
644 Bioinformatic analyses were performed in the Perseus software (Tyanova et al., 2016). Categorical
645 annotations were supplied in the form of Gene Ontology (GO) biological process (BP), molecular
646 function (MF), and cellular component (CC), as well as UniProt Keywords, KEGG and REACTOME
647 pathways. All annotations were extracted from the UniProt database. Quantified proteins were filtered
648 to have at least 4 valid values in at least one time point. Missing data were imputed by drawing
649 random numbers from a Gaussian distribution with a standard deviation of 30% and a downshift of
650 1.8 standard deviations from the mean. The imputed values have been tuned in order to simulate the
651 distribution of lowly abundant proteins. To identify differentially regulated proteins and acetyl-sites,
652 two-tailed paired *t*-tests were performed with a permutation-based false discovery correction applied
653 (FDR = 0.05). In the acetylome, an additional analysis was performed to expand the identification of
654 differentially expressed proteins, whereby an *a posteriori* information fusion scheme combining the
655 biological relevance (fold change) and the statistical significance (p-value), was implemented, as
656 previously described (Xiao et al., 2014). A Π-value significance score cut-off of 0.05 was selected.
657 Alterations to organelles were assessed using summed total protein abundances (Wisniewski, 2017)

658 and two-tailed paired t-tests ($p < 0.05$). Comparisons between individual proteins measured via
659 immunoblotting were performed using two-tailed paired t-tests ($p < 0.05$). Hierarchical clustering
660 analysis was performed on z-scored differentially regulated proteins using Euclidean distance.
661 Enrichment analyses were performed on differentially regulated proteins and acetyl-sites using
662 Fisher's exact tests and the application of a Benjamini-Hochberg false discovery correction (FDR =
663 0.02), as is the default setting in the Perseus software (Tyanova et al., 2016). Motif enrichment was
664 performed on upregulated acetyl-sites using iceLogo ($p < 0.01$) (Colaert et al., 2009). One-
665 dimensional enrichment analyses were performed as previously described (Juergen Cox & Mann,
666 2012). To analyze the relative stoichiometries of acetylated proteins in Fig. 4 abundance corrected
667 intensities (ACIs) were calculated for each acetyl-peptide by dividing the acetyl-peptide intensity by
668 the intensity of the corresponding protein in the proteome. Enrichment analyses were performed
669 against a background of all quantified proteins or acetyl-sites, except for hierarchical clustering
670 analyses where clusters were compared within the z-scored differentially regulated matrix. To
671 visualize complexes and functional protein-interactions in Fig. 6, protein interaction networks were
672 mapped using the STRING database, using an overall confidence cutoff of 0.7 without limiting the
673 number of interactions (Szklarczyk et al., 2019), and further processed with Cytoscape
674 (www.cytoscape.org).
675
676 *Cell culture*
677 The mouse skeletal muscle cell line C2C12 (CRL1772, ATCC) was seeded into six-well plates at a
678 density of 10^5 cells per well. Cells were cultured in growth medium (Dulbeccoo's modified Eagle's
679 medium containing 25 mM glucose, supplemented with 10% fetal bovine serum (FBS) and 1%.
680 Penicillin-streptomycin) at 37°C and 5% CO_2. Once the cells reached ~90% confluency,
681 differentiation was induced by replacing the FBS with 2% horse serum. On day 4 of differentiation,

682 cells were transfected with 25mM EP300 siRNA or scramble control siRNA via the TransIT-X2
683 Dynamic Delivery System (Mirus Bio), following the manufacturer's instructions. Cells were
684 harvested in 2% SDS on Day 6. Samples were immediately boiled at 95°C, sonicated in a Diagenode
685 Bioruptor water bath sonicator (15 x 30s intervals), and centrifuged at 16000g for 10 min. The pellet
686 was discarded and the supernatant was taken and used for immunoblotting analyses.
687
688 *Immunoblotting*
689 For human skeletal muscle immunoblot analyses, a fresh batch of ice-cold homogenization buffer
690 (10% glycerol, 20 mM Na-pyrophosphate, 150 mM NaCl, 50 mM HEPES (pH 7.5), 1% NP-40, 20
691 mM β-glycerophosphate, 2 mM Na_3VO_4, 10 mM NaF, 2 mM PMSF, 1 mM EDTA (pH 8), 1 mM
692 EGTA (pH 8), 10 $\mu g \cdot mL^{-1}$ Aprotinin, 10 $\mu g \cdot mL^{-1}$ Leupeptin and 3 mM Benzamidine) was prepared
693 and 80 µL added to 1 mg of freeze-dried and dissected muscle tissue. The tissue was homogenized
694 for 1 min at 28.5 Hz in a TissueLyser (Qiagen TissueLyser II, Retsch GmbH, Germany) before
695 samples were rotated end over end for 1 hour at 4°C and centrifuged at 18320g for 20 min at 4°C.
696 The pellet was discarded and the supernatant was taken and used for immunoblotting analyses. Total
697 protein concentration in the samples was determined with a standard BSA kit (Millipore). 15 µL of
698 the sample was diluted with 60 µL ultrapure water in order to keep the concentration within the linear
699 range of the calibration curve (0.2 to 2 $\mu g \cdot \mu L^{-1}$). The protein concentration of each sample was
700 adjusted by the addition of 6 × Laemmli buffer (7 mL 0.5M Tris-base, 3 mL glycerol, 0.93 g DTT, 1
701 g SDS and 1.2 mg bromophenol blue) and ultrapure water to reach equal concentrations (1.5 µg total
702 protein$\cdot \mu L^{-1}$). Human skeletal muscle standard samples (Ctrl) were obtained as a pool of all samples
703 included in the experiment.
704

705 Equal amounts of total protein were loaded on 10% TGX Stain-Free, 4-20% TGX Stain-Free, or
706 16.5% Criterion Tris-Tricine/Peptide gels (Bio-Rad) alongside two protein markers (Precision plus
707 all blue and dual color standards, Bio-Rad), three human skeletal muscle control samples and a four-
708 point standard curve (skeletal muscle samples of increasing volume). After standard SDS-page gel
709 electrophoresis proteins were semi-dry transferred to a PVDF membrane. Membranes were blocked
710 with either 2% skimmed milk or 3% BSA in Tris-buffered saline with 0.1% Tween-20 (TBST) before
711 overnight incubation with primary antibody. Afterwards, the membranes were washed in TBST,
712 incubated for 1 hour in HRP conjugated secondary antibody at room temperature and washed 3 × 15
713 min in TBST before the bands were visualized with an enhanced chemiluminescent reaction
714 (Immobilon Forte Western HRP substrate, Millipore) and signals recorded with a digital camera
715 (ChemiDoc MP Imaging System, Bio-Rad). Densitometry quantification of the immunoblotting band
716 intensities was done using Image Lab version 4 (Bio-Rad) and determined as the total band intensity
717 adjusted for the background intensity. The standard curve on each gel was used to confirm that the
718 loaded amount of protein in samples was capable of determining differences between samples by the
719 signal intensity being on the linear part of the standard curve. The variation of the triplicate human
720 standard sample signal loaded was used to evaluate equal transfer of proteins across each gel.
721 Coomassie staining was conducted to confirm equal loading and transfer of total protein from the
722 different samples. Immunoblotting of biological samples was performed in singleton.
723
724 Listed are the primary antibodies used and, where appropriate, their size of migration. Acetyl-lysine:
725 #9441, Cell Signaling Technologies; EP300: #sc48343, Santa Cruz Biotechnology, 300 kDa; ac-H2B
726 K20: #ab177430, Abcam, 14 kDa; H2B: #12364, Cell Signaling Technologies, 14 kDa; ac-H3 K23:
727 #14932, Cell Signaling Technologies, 17 kDa; H3: #4499, Cell Signaling Technologies, 17 kDa;
728 MYLK2: PA5-29324, Invitrogen, 65 kDa; OXPHOS antibody cocktail: ab110411, Abcam, 15-55

729 kDa; SIRT1: 07-131, Millipore, 80 kDa; SIRT3: #5490, Cell Signaling Technologies, 28 kDa; SIRT5:
730 #8782, Cell Signaling Technologies, 30 kDa; SIRT6: #12486, Cell Signaling Technologies, 36-42
731 kDa. The anti-GCN5L1 antibody (15 kDa) was a kind gift from Iain Scott, PhD, University of
732 Pittsburgh (Scott, Webster, Li, & Sack, 2012; Thapa et al., 2020). HRP conjugated goat anti-rabbit
733 (4010-05, SouthernBiotech) and a goat anti-mouse (P0447, DAKO Denmark) were used as secondary
734 antibodies.
735
736 *Statistical analyses*
737 For non-omics analyses, two-tailed paired t-tests were applied to assess the effect of HIIT, except for
738 substrate oxidation analyses whereby a mixed linear model was performed. Independent samples two-
739 tailed t-tests were used to assess the effect of EP300 KD on histone acetylation. Significance was
740 accepted as $p < 0.05$.
741

742 **Acknowledgements**

743 This work was supported by an unconditional donation from the Novo Nordisk Foundation (NNF) to
744 NNF Center for Basic Metabolic Research (http://www.cbmr.ku.dk) (Grant number
745 NNF18CC0034900), NNF Center for Protein Research (https://www.cpr.ku.dk/) (Grant number
746 NNF14CC001), and Team Denmark. We would like to acknowledge Matthias Mann, Jens Jung
747 Nielsen, Rebeca Soria Romero and the mass spectrometry platform from at the NNF Center for
748 Protein Research for technical assistance and access to mass spectrometers. We would like to thank
749 Iain Scott from the University of Pittsburgh Department of Medicine for the kind gift of the anti-
750 GCN5L1 antibody.

751

752 **Author contributions**

753 **Conceptualization**: M.H., A.S.D., A.K.L. and J.B. **Data curation**: A.S.D., M.H., A.K.L. and B.S.
754 **Formal analysis**: B.S., A.K.L., M.H., M.T., J.K.L. and A.S.D. **Funding acquisition**: A.S.D., M.H.
755 and J.B. **Investigation**: B.S., A.K.L., M.H., M.T., A.G., J.K.L., J.P.Q. and A.S.D. **Methodology**:
756 M.H., A.S.D., A.K.L., B.S., J.K.L., A.G., J.P.Q. and J.B. **Project administration**: M.H. and A.S.D.
757 **Resources**: A.S.D., M.H. and J.B. **Supervision**: A.S.D. and M.H. **Validation**: M.T., B.S., A.K.L.,
758 M.H. and A.S.D. **Visualization**: B.S. **Writing – Original draft**: B.S., M.H., A.K.L. and A.S.D.
759 **Writing – review and editing**: M.H., A.K.L., B.S., A.G., J.K.L., J.P.Q., M.T., B.W., J.B. and A.S.D.

760

761 **Competing interests**

762 The authors declare no competing interests.

763

764 **Materials & Correspondence**

765 Requests for reagents and resources should be directed to Atul S. Deshmukh (atul.deshmukh@sund.ku.dk).

766 **Supplementary Tables**
767
768 ***Table S1.*** *Identified proteins.*
769
770 ***Table S2.*** *Quantified proteins and their regulation by HIIT.*
771
772 ***Table S3.*** *Fisher's exact test of HIIT-regulated proteins (FDR < 0.05).*
773
774 ***Table S4.*** *Identified acetyl-sites.*
775
776 ***Table S5.*** *Quantified acetyl-sites and their regulation by HIIT.*
777
778 ***Table S6.*** *Summed acetylation intensity per protein.*
779
780 ***Table S7.*** *One-dimensional enrichment analysis of summed acetylation intensity.*
781
782 ***Table S8.*** ***A****bundance corrected intensities (ACIs) of acetyl-sites pre-HIIT.*
783
784 ***Table S9.*** *One-dimensional enrichment analysis of pre-HIIT acetyl-site ACI (Leading protein IID*
785 *was used for relative enrichment).*
786
787 ***Table S10.*** *Fisher's exact test of HIIT-regulated (ΠI < 0.05) acetyl-sites (Leading protein IID was*
788 *used for relative enrichment).*
789
790 https://drive.google.com/drive/folders/13Hx0NcA66gY6Fl-5L3NjFov0F4KoH36H?usp=sharing
791
792

793 **Figure Legends**

794 ***Figure 1.*** **Physiological adaptations to HIIT**

795 **A**. Experimental overview. **B**. Subject characteristics. **C**. Five weeks of HIIT increased maximal
796 oxygen uptake ($\dot{V}O_{2max}$) and incremental peak power output (iPPO). **D** HIIT increased whole-body
797 fat oxidation during submaximal exercise (50-150 W) without altering **E**. carbohydrate oxidation. **F**.
798 HIIT increased mitochondrial respiration in skeletal muscle (L_N: leak respiration, FAO: fatty acid
799 oxidation, CI_D: submaximal CI respiration, P_D: submaximal CI+II respiration, P: oxidative
800 phosphorylation capacity, E: electron transport system capacity, E_{CII}: succinate-supported electron
801 transport system capacity). **G**. HIIT increased skeletal muscle citrate synthase (CS) activity. **H**.
802 Analytical workflow. Summary statistics are mean ± SEM (n = 8). * $p < 0.05$, ** $p < 0.01$, *** $p <$
803 0.001.

804

805 ***Figure 2.*** **HIIT increases mitochondrial proteins and reduces a subset of contractile fiber**
806 **associated proteins**

807 **A**. Volcano plot displaying 102 upregulated and 24 downregulated proteins following HIIT (FDR <
808 0.05). **B**. Fisher's exact tests identified the enrichment of mitochondrial terms within the differentially
809 regulated proteins (enrichment analysis FDR < 0.02). **C**. Hierarchical clustering and enrichment
810 analysis (enrichment analysis FDR < 0.02) on differentially regulated proteins identified that
811 mitochondrial terms are enriched within the upregulated proteins, while cytoplasm (UniProt
812 Keyword) is enriched amongst the downregulated proteins. **D**. Summed total protein abundances for
813 different organelles (UniProt Keyword) shows upregulation of the mitochondrial protein content. **E-**
814 **G**. Summed total protein abundances display upregulation of electron transport chain complexes (**E**.),
815 mitochondrially-encoded proteins (**F**.) and proteins with a transit peptide (**G**.). Summary statistics are
816 mean ± SEM (n = 8). * $p < 0.05$, ** $p < 0.01$, *** $p < 0.001$.

817

818 ***Figure 3.*** **HIIT regulates proteins involved in skeletal muscle calcium sensitivity and handling**

819 HIIT did not alter the abundance of myosin heavy chain (MYH1: MyHC2x, MYH2: MyHC2a,
820 MYH4: MyHC2x, MYH7: MyHCβ; **A**.) or light chain (**B**.) isoforms. **C**. HIIT regulates proteins
821 controlling myosin phosphorylation. **D**. HIIT reduces abundance of subunits of the dihydropyridine
822 receptor. **E**. Summed total protein abundances display downregulation of the dihydropyridine
823 receptor. **F**. HIIT does not alter the abundance of ryanodine receptor 1. Summary statistics are mean
824 ± SEM (n = 8). ^ FDR < 0.05. * p < 0.05, ** p < 0.01, *** p < 0.001.

825

826 ***Figure 4.*** **The human skeletal muscle acetylome displays higher stoichiometry on mitochondrial**
827 **proteins and lower stoichiometry on contractile proteins**

828 **A**. We quantified 1263 acetyl-sites corresponding to 464 proteins (n = 7). Of these, 421 proteins were
829 also quantified in the proteome with 1232 of the quantified acetyl-sites located on these 421 proteins.
830 **B**. Distribution of acetyl-sites on proteins within the pre-HIIT acetylome. **C**. Top 10 highest intensity
831 acetylated proteins (acetyl-peptide intensities were summed for each protein) within the pre-HIIT
832 acetylome. **D**. Cumulative protein abundance and rank within the proteome (the top 10 highest
833 intensity acetyl-proteins are highlighted). **E**. One-dimensional enrichment analysis of acetylated
834 protein intensity identified mitochondrial proteins, particularly those involved in carboxylic acid
835 metabolism and monovalent inorganic cation transport (e.g. complex V) as having systematically
836 high acetylation intensities (enrichment analysis FDR < 0.02). **F**. Top 10 acetyl-sites with highest
837 abundance-corrected intensities (ACIs). **G**. One-dimensional enrichment analysis of acetyl-site ACIs
838 identified mitochondrial and carboxylic acid catabolic proteins as higher stoichiometry (positive
839 enrichment factor), while contractile fiber cytosolic and plasma membrane proteins were enriched
840 as lower stoichiometry (negative enrichment factor; (enrichment analysis FDR < 0.02; enrichment

841 performed on leading protein IDs). **H**. Histogram depicting the ACI distribution of the total acetylome
842 (blue), the mitochondrial acetyl-sites (green) and the contractile fiber acetyl-sites (yellow).
843 Mitochondrial proteins were distributed at higher ACI values and contractile fiber proteins at lower
844 ACI values than the total acetylome.
845
846 ***Figure 5*. HIIT increases acetylation of mitochondrial and TCA cycle proteins concomitantly**
847 **with an increase in SIRT3 abundance**
848 **A**. Volcano plot displaying 20 upregulated (filled red circles) and 1 downregulated (filled blue circle)
849 acetyl-sites following HIIT at an FDR < 0.05, while 257 acetyl-sites were upregulated (red circles)
850 and 26 downregulated (blue circles) at Π < 0.05 (n = 7). **B**. Scatter plot indicating that HIIT-induced
851 changes in acetyl-site intensity typically exceeded that of the corresponding protein. **C**. Fisher's exact
852 tests identified the enrichment of mitochondrial and TCA cycle terms within the differentially
853 regulated acetyl-proteins (enrichment analysis FDR < 0.02; enrichment performed on leading protein
854 IDs). **D**. IceLogo motif enrichment (p < 0.01) for the upregulated sites displayed a predominance of
855 proximal cysteine residues relative to the acetylated lysine (position 0). **E**. Immunoblotting analysis
856 identified the upregulation of the deacetylases SIRT3, SIRT5, and SIRT6, but no change in SIRT1,
857 whilst the mitochondrial acetyltransferase GCN5L1 remained unchanged following HIIT (n = 7-8).
858 Representative images confirming equal loading are displayed in Fig S5. * p < 0.05, ** p < 0.01, ***
859 p < 0.001.
860
861 ***Figure 6*. Individual acetyl-site regulation of mitochondrial, TCA cycle and contractile proteins**
862 **following HIIT**

863 Regulation of acetyl-sites on **A**. electron transport chain complex subunits (annotated by HUGO), **B**.
864 TCA cycle proteins (annotated by KEGG) and **C**. muscle contraction proteins (annotated by
865 REACTOME).
866
867 ***Figure 7.*** **HIIT increases acetylation on specific histone acetyl-sites**
868 HIIT increased acetylation on **A**. H1.5 K48, **B**. H2B type 2F K16/20 and **C**. H3 K23. **D**. HIIT did not
869 alter H4 acetylation (n = 7). **E.** Knockdown of EP300 reduces acetylation of H2B K20 but not H3
870 K23 in C2C12 myotubes (n = 3). Representative images confirming equal loading are displayed in
871 Fig S5. Summary statistics are mean ± SEM. † $\Pi < 0.05$. * $p < 0.05$, ** $p < 0.01$, *** $p < 0.001$.
872
873 ***Figure S1.*** **Proteome quality control**
874 **A**. Quantified proteins from each sample. **B**. Representative Pearson correlation between biological
875 replicates (Pre 4 v Pre 5). **C**. Cellular compartment (GOCC) coverage of the proteome. **D**. Principal
876 component analysis of the proteome. P: participant.
877
878 ***Figure S2.*** **HIIT increases electron transport chain subunits**
879 Immunoblotting analyses confirmed the upregulation of electron transport chain proteins.
880 Representative images confirming equal loading are displayed in Fig S5. Summary statistics are mean
881 ± SEM (n = 8). * $p < 0.05$, ** $p < 0.01$, *** $p < 0.001$.
882
883 ***Figure S3***. **HIIT decreases MYLK2 abundance**
884 **A**. Immunoblotting analysis confirms the downregulation of MYLK2. Representative images
885 confirming equal loading are displayed in Fig S5. **B**. No change in the abundance of

886 sarcoplasmic/endoplasmic reticulum calcium ATPases 1-3 (SERCAs). Summary statistics are mean
887 ± SEM (n = 8). * $p < 0.05$, ** $p < 0.01$, *** $p < 0.001$.
888
889 ***Figure S4.*** **Acetylome quality control**
890 **A**. Overlap between identified acetyl-site with those identified in human skeletal muscle by Lundby
891 et al. (2012). **B**. Quantified acetyl-sites from each sample. **C**. Representative Pearson correlation
892 between biological replicates (Pre 4 v Pre 5). **D**. Cellular compartment (GOCC) coverage of the
893 acetylome. **E**. Principal component analysis of the acetylome. P: participant. **F**. Immunoblotting
894 analysis confirmed the upregulation of acetylation following HIIT (n = 7). Representative images
895 confirming equal loading are displayed in Fig S5. * $p < 0.05$, ** $p < 0.01$, *** $p < 0.001$.
896
897 ***Figure S5.*** **Representative images of equal loading for immunoblot analyses**
898 **A**. Coomassie stain for n = 8 immunoblots of human skeletal muscle (Fig 5E (SIRT1-6), S2, and
899 S3A). **B**. Stain-free image for n = 7 immunoblots of human skeletal muscle (Fig 5E (GCN5L1), and
900 S4F). **C**. Stain-free image for EP300 KD immunoblots (Fig 7E).
901
902 ***Figure S6.*** **CONSORT flow diagram of enrolled participants**

References

Alessi, D., MacDougall, L. K., Sola, M. M., Ikebe, M., & Cohen, P. (1992). The control of protein phosphatase-1 by targetting subunits. The major myosin phosphatase in avian smooth muscle is a novel form of protein phosphatase-1. *European Journal of Biochemistry, 210*(3), 1023-1035. doi:10.1111/j.1432-1033.1992.tb17508.x

Baeza, J., Smallegan, M. J., & Denu, J. M. (2016). Mechanisms and Dynamics of Protein Acetylation in Mitochondria. *Trends in Biochemical Sciences, 41*(3), 231-244. doi:10.1016/j.tibs.2015.12.006

Banas, K., Clow, C., Jasmin, B. J., & Renaud, J. M. (2011). The KATP channel Kir6.2 subunit content is higher in glycolytic than oxidative skeletal muscle fibers. *American Journal of Physiology: Regulatory, Integrative and Comparative Physiology, 301*(4), R916-925. doi:10.1152/ajpregu.00663.2010

Berg, H. E., Tedner, B., & Tesch, P. A. (1993). Changes in lower limb muscle cross-sectional area and tissue fluid volume after transition from standing to supine. *Acta Physiologica Scandinavica, 148*(4), 379-385. doi:10.1111/j.1748-1716.1993.tb09573.x

Braschi, B., Denny, P., Gray, K., Jones, T., Seal, R., Tweedie, S., . . . Bruford, E. (2019). Genenames.org: the HGNC and VGNC resources in 2019. *Nucleic Acids Research, 47*(D1), D786-D792. doi:10.1093/nar/gky930

Bruderer, R., Bernhardt, O. M., Gandhi, T., Miladinović, S. M., Cheng, L. Y., Messner, S., . . . Reiter, L. (2015). Extending the limits of quantitative proteome profiling with data-independent acquisition and application to acetaminophen-treated three-dimensional liver microtissues. *Molecular & Cellular Proteomics, 14*(5), 1400-1410. doi:10.1074/mcp.M114.044305

Campanella, M., Casswell, E., Chong, S., Farah, Z., Wieckowski, M. R., Abramov, A. Y., . . . Duchen, M. R. (2008). Regulation of Mitochondrial Structure and Function by the F1Fo-ATPase Inhibitor Protein, IF1. *Cell Metabolism, 8*(1), 13-25. doi:10.1016/j.cmet.2008.06.001

Cerniglia, L. M., Delmonico, M. J., Lindle, R., Hurley, B. F., & Rogers, M. A. (2007). Effects of acute supine rest on mid-thigh cross-sectional area as measured by computed tomography. *Clinical Physiology and Functional Imaging, 27*(4), 249-253. doi:10.1111/j.1475-097X.2007.00742.x

Chen, H., Ruiz, P. D., Novikov, L., Casill, A. D., Park, J. W., & Gamble, M. J. (2014). MacroH2A1.1 and PARP-1 cooperate to regulate transcription by promoting CBP-mediated H2B acetylation. *Nature Structural & Molecular Biology, 21*(11), 981-989. doi:10.1038/nsmb.2903

Chen, Y., Deng, Y., Zhang, J., Yang, L., Xie, X., & Xu, T. (2009). GDI-1 preferably interacts with Rab10 in insulin-stimulated GLUT4 translocation. *Biochemical Journal, 422*(2), 229-235. doi:10.1042/bj20090624

Choudhary, C., Weinert, B. T., Nishida, Y., Verdin, E., & Mann, M. (2014). The growing landscape of lysine acetylation links metabolism and cell signalling. *Nature Reviews Molecular Cell Biology, 15*(8), 536-550. doi:10.1038/nrm3841

Christensen, P. M., Jacobs, R. A., Bonne, T., Flück, D., Bangsbo, J., & Lundby, C. (2016). A short period of high-intensity interval training improves skeletal muscle mitochondrial function and pulmonary oxygen uptake kinetics. *J Appl Physiol (1985), 120*(11), 1319-1327. doi:10.1152/japplphysiol.00115.2015

Cohen, P. (2000). The regulation of protein function by multisite phosphorylation--a 25 year update. *Trends in Biochemical Sciences, 25*(12), 596-601. doi:10.1016/s0968-0004(00)01712-6

Colaert, N., Helsens, K., Martens, L., Vandekerckhove, J., & Gevaert, K. (2009). Improved visualization of protein consensus sequences by iceLogo. *Nat Methods, 6*(11), 786-787. doi:10.1038/nmeth1109-786

951 Constantin-Teodosiu, D., Carlin, J. I., Cederblad, G., Harrist, R. C., & Hultman, E. (1991). Acetyl
952 group accumulation and pyruvate dehydrogenase activity in human muscle during
953 incremental exercise. *Acta Physiologica Scandinavica, 143*(4), 367-372. doi:10.1111/j.1748-
954 1716.1991.tb09247.x
955 Constantin-Teodosiu, D., Constantin, D., Stephens, F., Laithwaite, D., & Greenhaff, P. L. (2012).
956 The role of FOXO and PPAR transcription factors in diet-mediated inhibition of PDC
957 activation and carbohydrate oxidation during exercise in humans and the role of
958 pharmacological activation of PDC in overriding these changes. *Diabetes, 61*(5), 1017-1024.
959 doi:10.2337/db11-0799
960 Cox, J., & Mann, M. (2008). MaxQuant enables high peptide identification rates, individualized
961 p.p.b.-range mass accuracies and proteome-wide protein quantification. *Nature*
962 *Biotechnology, 26*(12), 1367-1372. doi:10.1038/nbt.1511
963 Cox, J., & Mann, M. (2012). 1D and 2D annotation enrichment: a statistical method integrating
964 quantitative proteomics with complementary high-throughput data. *BMC Bioinformatics, 13*
965 *Suppl 16*(Suppl 16), S12-S12. doi:10.1186/1471-2105-13-S16-S12
966 Davis, J. S., Hassanzadeh, S., Winitsky, S., Lin, H., Satorius, C., Vemuri, R., . . . Epstein, N. D.
967 (2001). The overall pattern of cardiac contraction depends on a spatial gradient of myosin
968 regulatory light chain phosphorylation. *Cell, 107*(5), 631-641. doi:10.1016/s0092-
969 8674(01)00586-4
970 Deshmukh, A. S., Murgia, M., Nagaraj, N., Treebak, J. T., Cox, J., & Mann, M. (2015). Deep
971 proteomics of mouse skeletal muscle enables quantitation of protein isoforms, metabolic
972 pathways, and transcription factors. *Molecular & Cellular Proteomics, 14*(4), 841-853.
973 doi:10.1074/mcp.M114.044222
974 Deshmukh, A. S., Steenberg, D. E., Hostrup, M., Birk, J. B., Larsen, J. K., Santos, A., . . .
975 Wojtaszewski, J. F. P. (2021). Deep muscle-proteomic analysis of freeze-dried human muscle
976 biopsies reveals fiber type-specific adaptations to exercise training. *Nature Communications,*
977 *12*(1), 304. doi:10.1038/s41467-020-20556-8
978 Deutscher, M. P. (1984). The eucaryotic aminoacyl-tRNA synthetase complex: suggestions for its
979 structure and function. *The Journal of Cell Biology, 99*(2), 373-377. doi:10.1083/jcb.99.2.373
980 Dohlmann, T. L., Hindsø, M., Dela, F., Helge, J. W., & Larsen, S. (2018). High-intensity interval
981 training changes mitochondrial respiratory capacity differently in adipose tissue and skeletal
982 muscle. *Physiological Reports, 6*(18), e13857. doi:10.14814/phy2.13857
983 Egan, B., & Zierath, J. R. (2013). Exercise metabolism and the molecular regulation of skeletal
984 muscle adaptation. *Cell Metabolism, 17*(2), 162-184. doi:10.1016/j.cmet.2012.12.012
985 Flucher, B. E., & Franzini-Armstrong, C. (1996). Formation of junctions involved in excitation-
986 contraction coupling in skeletal and cardiac muscle. *Proceedings of the National Academy of*
987 *Sciences of the United States of America, 93*(15), 8101-8106. doi:10.1073/pnas.93.15.8101
988 Foster, D. B., Liu, T., Rucker, J., O'Meally, R. N., Devine, L. R., Cole, R. N., & O'Rourke, B. (2013).
989 The Cardiac Acetyl-Lysine Proteome. *PloS One, 8*(7), e67513.
990 doi:10.1371/journal.pone.0067513
991 Freeman, H. C., Hugill, A., Dear, N. T., Ashcroft, F. M., & Cox, R. D. (2006). Deletion of
992 Nicotinamide Nucleotide Transhydrogenase. *Diabetes, 55*(7), 2153. doi:10.2337/db06-0358
993 Gibala, M. J., MacLean, D. A., Graham, T. E., & Saltin, B. (1998). Tricarboxylic acid cycle
994 intermediate pool size and estimated cycle flux in human muscle during exercise. *American*
995 *Journal of Physiology, 275*(2), E235-242. doi:10.1152/ajpendo.1998.275.2.E235
996 Gonzalez-Franquesa, A., Stocks, B., Chubanava, S., Hattel, H. B., Moreno-Justicia, R., Peijs, L., . . .
997 Deshmukh, A. S. (2021). Mass-spectrometry-based proteomics reveals mitochondrial
998 supercomplexome plasticity. *Cell Rep, 35*(8), 109180. doi:10.1016/j.celrep.2021.109180

Granata, C., Oliveira, R. S., Little, J. P., Renner, K., & Bishop, D. J. (2016). Training intensity modulates changes in PGC-1alpha and p53 protein content and mitochondrial respiration, but not markers of mitochondrial content in human skeletal muscle. *FASEB Journal, 30*(2), 959-970. doi:10.1096/fj.15-276907

Hansen, B. K., Gupta, R., Baldus, L., Lyon, D., Narita, T., Lammers, M., . . . Weinert, B. T. (2019). Analysis of human acetylation stoichiometry defines mechanistic constraints on protein regulation. *Nature Communications, 10*(1), 1055. doi:10.1038/s41467-019-09024-0

Hebert, A. S., Dittenhafer-Reed, K. E., Yu, W., Bailey, D. J., Selen, E. S., Boersma, M. D., . . . Coon, J. J. (2013). Calorie restriction and SIRT3 trigger global reprogramming of the mitochondrial protein acetylome. *Molecular Cell, 49*(1), 186-199. doi:10.1016/j.molcel.2012.10.024

Hendzel, M. J., Sun, J. M., Chen, H. Y., Rattner, J. B., & Davie, J. R. (1994). Histone acetyltransferase is associated with the nuclear matrix. *Journal of Biological Chemistry, 269*(36), 22894-22901.

Hirschey, M. D., Shimazu, T., Goetzman, E., Jing, E., Schwer, B., Lombard, D. B., . . . Verdin, E. (2010). SIRT3 regulates mitochondrial fatty-acid oxidation by reversible enzyme deacetylation. *Nature, 464*(7285), 121-125. doi:10.1038/nature08778

Ho, H.-Y., Lin, Y.-T., Lin, G., Wu, P.-R., & Cheng, M.-L. (2017). Nicotinamide nucleotide transhydrogenase (NNT) deficiency dysregulates mitochondrial retrograde signaling and impedes proliferation. *Redox Biology, 12*, 916-928. doi:https://doi.org/10.1016/j.redox.2017.04.035

Hoek, J. B., & Rydström, J. (1988). Physiological roles of nicotinamide nucleotide transhydrogenase. *Biochemical Journal, 254*(1), 1-10. doi:10.1042/bj2540001

Hoffman, N. J., Parker, B. L., Chaudhuri, R., Fisher-Wellman, K. H., Kleinert, M., Humphrey, S. J., . . . James, D. E. (2015). Global phosphoproteomic analysis of human skeletal muscle reveals a network of exercise-regulated kinases and AMPK substrates. *Cell Metabolism, 22*(5), 922-935. doi:10.1016/j.cmet.2015.09.001

Holloway, K. V., O'Gorman, M., Woods, P., Morton, J. P., Evans, L., Cable, N. T., . . . Burniston, J. G. (2009). Proteomic investigation of changes in human vastus lateralis muscle in response to interval-exercise training. *Proteomics, 9*(22), 5155-5174. doi:10.1002/pmic.200900068

Hostrup, M., & Bangsbo, J. (2017). Limitations in intense exercise performance of athletes – effect of speed endurance training on ion handling and fatigue development. *The Journal of Physiology, 595*(9), 2897-2913. doi:10.1113/JP273218

Hostrup, M., Gunnarsson, T. P., Fiorenza, M., Mørch, K., Onslev, J., Pedersen, K. M., & Bangsbo, J. (2019). In-season adaptations to intense intermittent training and sprint interval training in sub-elite football players. *Scandinavian Journal of Medicine and Science in Sports, 29*(5), 669-677. doi:10.1111/sms.13395

Hostrup, M., Onslev, J., Jacobson, G. A., Wilson, R., & Bangsbo, J. (2018). Chronic β(2) -adrenoceptor agonist treatment alters muscle proteome and functional adaptations induced by high intensity training in young men. *Journal of Physiology, 596*(2), 231-252. doi:10.1113/jp274970

Howlett, R. A., Parolin, M. L., Dyck, D. J., Hultman, E., Jones, N. L., Heigenhauser, G. J., & Spriet, L. L. (1998). Regulation of skeletal muscle glycogen phosphorylase and PDH at varying exercise power outputs. *American Journal of Physiology, 275*(2 Pt 2), R418-425.

Jacobs, R. A., Flück, D., Bonne, T. C., Bürgi, S., Christensen, P. M., Toigo, M., & Lundby, C. (2013). Improvements in exercise performance with high-intensity interval training coincide with an increase in skeletal muscle mitochondrial content and function. *Journal of Applied Physiology, 115*(6), 785-793. doi:10.1152/japplphysiol.00445.2013

James, A. M., Smith, A. C., Smith, C. L., Robinson, A. J., & Murphy, M. P. (2018). Proximal Cysteines that Enhance Lysine N-Acetylation of Cytosolic Proteins in Mice Are Less

Conserved in Longer-Living Species. *Cell Rep, 24*(6), 1445-1455. doi:10.1016/j.celrep.2018.07.007

Jeukendrup, A. E., & Wallis, G. A. (2005). Measurement of substrate oxidation during exercise by means of gas exchange measurements. *International Journal of Sports Medicine, 26 Suppl 1*, S28-37. doi:10.1055/s-2004-830512

Jing, E., O'Neill, B. T., Rardin, M. J., Kleinridders, A., Ilkeyeva, O. R., Ussar, S., . . . Kahn, C. R. (2013). Sirt3 regulates metabolic flexibility of skeletal muscle through reversible enzymatic deacetylation. *Diabetes, 62*(10), 3404-3417. doi:10.2337/db12-1650

Joseph, J. S., Ayeleso, A. O., & Mukwevho, E. (2017). Exercise increases hyper-acetylation of histones on the Cis-element of NRF-1 binding to the Mef2a promoter: Implications on type 2 diabetes. *Biochemical and Biophysical Research Communications, 486*(1), 83-87. doi:https://doi.org/10.1016/j.bbrc.2017.03.002

Kulak, N. A., Geyer, P. E., & Mann, M. (2017). Loss-less Nano-fractionator for High Sensitivity, High Coverage Proteomics. *Molecular & Cellular Proteomics, 16*(4), 694-705. doi:10.1074/mcp.O116.065136

Larsen, S., Danielsen, J. H., Søndergård, S. D., Søgaard, D., Vigelsoe, A., Dybboe, R., . . . Helge, J. W. (2015). The effect of high-intensity training on mitochondrial fat oxidation in skeletal muscle and subcutaneous adipose tissue. *Scandinavian Journal of Medicine and Science in Sports, 25*(1), e59-e69. doi:10.1111/sms.12252

Larsen, S., Nielsen, J., Hansen, C. N., Nielsen, L. B., Wibrand, F., Stride, N., . . . Hey-Mogensen, M. (2012). Biomarkers of mitochondrial content in skeletal muscle of healthy young human subjects. *The Journal of Physiology, 590*(14), 3349-3360. doi:10.1113/jphysiol.2012.230185

Lee, P., Day, R. O., Greenfield, J. R., & Ho, K. K. (2013). Formoterol, a highly β2-selective agonist, increases energy expenditure and fat utilisation in men. *International Journal of Obesity (2005), 37*(4), 593-597. doi:10.1038/ijo.2012.90

Lochmann, T. L., Thomas, R. R., Bennett, J. P., Jr., & Taylor, S. M. (2015). Epigenetic Modifications of the PGC-1α Promoter during Exercise Induced Expression in Mice. *PloS One, 10*(6), e0129647. doi:10.1371/journal.pone.0129647

Lowry, O. (2012). *A flexible system of enzymatic analysis*: Elsevier.

Ludwig, C., Gillet, L., Rosenberger, G., Amon, S., Collins, B. C., & Aebersold, R. (2018). Data-independent acquisition-based SWATH-MS for quantitative proteomics: a tutorial. *Molecular Systems Biology, 14*(8), e8126. doi:10.15252/msb.20178126

Lundby, A., Lage, K., Weinert, B. T., Bekker-Jensen, D. B., Secher, A., Skovgaard, T., . . . Olsen, J. V. (2012). Proteomic analysis of lysine acetylation sites in rat tissues reveals organ specificity and subcellular patterns. *Cell Rep, 2*(2), 419-431. doi:10.1016/j.celrep.2012.07.006

Lv, D., Jia, F., Hou, Y., Sang, Y., Alvarez, A. A., Zhang, W., . . . Feng, H. (2017). Histone Acetyltransferase KAT6A Upregulates PI3K/AKT Signaling through TRIM24 Binding. *Cancer Research, 77*(22), 6190-6201. doi:10.1158/0008-5472.Can-17-1388

Lynch, G. S., McKenna, M. J., & Williams, D. A. (1994). Sprint-training effects on some contractile properties of single skinned human muscle fibres. *Acta Physiologica Scandinavica, 152*(3), 295-306. doi:10.1111/j.1748-1716.1994.tb09809.x

Majerczak, J., Karasinski, J., & Zoladz, J. A. (2008). Training induced decrease in oxygen cost of cycling is accompanied by down-regulation of SERCA expression in human vastus lateralis muscle. *Journal of Physiology and Pharmacology, 59*(3), 589-602.

Mandsager, K., Harb, S., Cremer, P., Phelan, D., Nissen, S. E., & Jaber, W. (2018). Association of Cardiorespiratory Fitness With Long-term Mortality Among Adults Undergoing Exercise Treadmill Testing. *JAMA Network Open, 1*(6), e183605-e183605. doi:10.1001/jamanetworkopen.2018.3605

McGee, S. L., Fairlie, E., Garnham, A. P., & Hargreaves, M. (2009). Exercise-induced histone modifications in human skeletal muscle. *Journal of Physiology, 587*(Pt 24), 5951-5958. doi:10.1113/jphysiol.2009.181065

Meinild Lundby, A. K., Jacobs, R. A., Gehrig, S., de Leur, J., Hauser, M., Bonne, T. C., . . . Lundby, C. (2018). Exercise training increases skeletal muscle mitochondrial volume density by enlargement of existing mitochondria and not de novo biogenesis. *Acta Physiol (Oxf), 222*(1), e12905-n/a. doi:10.1111/apha.12905

Munkvik, M., Rehn, T. A., Slettaløkken, G., Hasic, A., Hallén, J., Sjaastad, I., . . . Lunde, P. K. (2010). Training effects on skeletal muscle calcium handling in human chronic heart failure. *Medicine and Science in Sports and Exercise, 42*(5), 847-855. doi:10.1249/MSS.0b013e3181c29ec1

Murgia, M., Toniolo, L., Nagaraj, N., Ciciliot, S., Vindigni, V., Schiaffino, S., . . . Mann, M. (2017). Single Muscle Fiber Proteomics Reveals Fiber-Type-Specific Features of Human Muscle Aging. *Cell Rep, 19*(11), 2396-2409. doi:10.1016/j.celrep.2017.05.054

Nana, A., Slater, G. J., Hopkins, W. G., & Burke, L. M. (2012). Effects of Daily Activities on Dual-Energy X-ray Absorptiometry Measurements of Body Composition in Active People. *Medicine and Science in Sports and Exercise, 44*(1), 180-189. doi:10.1249/MSS.0b013e318228b60e

Narita, T., Weinert, B. T., & Choudhary, C. (2019). Functions and mechanisms of non-histone protein acetylation. *Nature Reviews: Molecular Cell Biology, 20*(3), 156-174. doi:10.1038/s41580-018-0081-3

Ortenblad, N., Lunde, P. K., Levin, K., Andersen, J. L., & Pedersen, P. K. (2000). Enhanced sarcoplasmic reticulum Ca(2+) release following intermittent sprint training. *American Journal of Physiology: Regulatory, Integrative and Comparative Physiology, 279*(1), R152-160. doi:10.1152/ajpregu.2000.279.1.R152

Overmyer, K. A., Evans, C. R., Qi, N. R., Minogue, C. E., Carson, J. J., Chermside-Scabbo, C. J., . . . Burant, C. F. (2015). Maximal oxidative capacity during exercise is associated with skeletal muscle fuel selection and dynamic changes in mitochondrial protein acetylation. *Cell Metabolism, 21*(3), 468-478. doi:10.1016/j.cmet.2015.02.007

Parker, B. L., Kiens, B., Wojtaszewski, J. F. P., Richter, E. A., & James, D. E. (2020). Quantification of exercise-regulated ubiquitin signaling in human skeletal muscle identifies protein modification cross talk via NEDDylation. *FASEB Journal, 34*(4), 5906-5916. doi:https://doi.org/10.1096/fj.202000075R

Parra, M. A., Kerr, D., Fahy, D., Pouchnik, D. J., & Wyrick, J. J. (2006). Deciphering the roles of the histone H2B N-terminal domain in genome-wide transcription. *Molecular and Cellular Biology, 26*(10), 3842-3852. doi:10.1128/MCB.26.10.3842-3852.2006

Pathiraja, T. N., Thakkar, K. N., Jiang, S., Stratton, S., Liu, Z., Gagea, M., . . . Barton, M. C. (2015). TRIM24 links glucose metabolism with transformation of human mammary epithelial cells. *Oncogene, 34*(22), 2836-2845. doi:10.1038/onc.2014.220

Pesta, D., & Gnaiger, E. (2012). High-resolution respirometry: OXPHOS protocols for human cells and permeabilized fibers from small biopsies of human muscle. *Methods in Molecular Biology, 810*, 25-58. doi:10.1007/978-1-61779-382-0_3

Pesta, D., Hoppel, F., Macek, C., Messner, H., Faulhaber, M., Kobel, C., . . . Gnaiger, E. (2011). Similar qualitative and quantitative changes of mitochondrial respiration following strength and endurance training in normoxia and hypoxia in sedentary humans. *American Journal of Physiology: Regulatory, Integrative and Comparative Physiology, 301*(4), R1078-R1087. doi:10.1152/ajpregu.00285.2011

Pietrocola, F., Galluzzi, L., Bravo-San Pedro, José M., Madeo, F., & Kroemer, G. (2015). Acetyl Coenzyme A: A Central Metabolite and Second Messenger. *Cell Metabolism, 21*(6), 805-821. doi:https://doi.org/10.1016/j.cmet.2015.05.014

Pougovkina, O., te Brinke, H., Ofman, R., van Cruchten, A. G., Kulik, W., Wanders, R. J., . . . de Boer, V. C. (2014). Mitochondrial protein acetylation is driven by acetyl-CoA from fatty acid oxidation. *Human Molecular Genetics, 23*(13), 3513-3522. doi:10.1093/hmg/ddu059

Putman, C. T., Jones, N. L., Hultman, E., Hollidge-Horvat, M. G., Bonen, A., McConachie, D. R., & Heigenhauser, G. J. F. (1998). Effects of short-term submaximal training in humans on muscle metabolism in exercise. *American Journal of Physiology-Endocrinology and Metabolism, 275*(1), E132-E139. doi:10.1152/ajpendo.1998.275.1.E132

Rappsilber, J., Mann, M., & Ishihama, Y. (2007). Protocol for micro-purification, enrichment, pre-fractionation and storage of peptides for proteomics using StageTips. *Nature Protocols, 2*(8), 1896-1906. doi:10.1038/nprot.2007.261

Ribas, V., Drew, B. G., Zhou, Z., Phun, J., Kalajian, N. Y., Soleymani, T., . . . Hevener, A. L. (2016). Skeletal muscle action of estrogen receptor α is critical for the maintenance of mitochondrial function and metabolic homeostasis in females. *Science Translational Medicine, 8*(334), 334ra354. doi:10.1126/scitranslmed.aad3815

Robinson, M. M., Dasari, S., Konopka, A. R., Johnson, M. L., Manjunatha, S., Esponda, R. R., . . . Nair, K. S. (2017). Enhanced protein translation underlies improved metabolic and physical adaptations to different exercise training modes in young and old humans. *Cell Metabolism, 25*(3), 581-592. doi:10.1016/j.cmet.2017.02.009

Scott, I., Webster, B. R., Li, J. H., & Sack, M. N. (2012). Identification of a molecular component of the mitochondrial acetyltransferase programme: a novel role for GCN5L1. *The Biochemical Journal, 443*(3), 655-661. doi:10.1042/BJ20120118

Smith, J. A., Kohn, T. A., Chetty, A. K., & Ojuka, E. O. (2008). CaMK activation during exercise is required for histone hyperacetylation and MEF2A binding at the MEF2 site on the Glut4 gene. *American Journal of Physiology-Endocrinology and Metabolism, 295*(3), E698-704. doi:10.1152/ajpendo.00747.2007

St Clair, D. K., Wan, X. S., Oberley, T. D., Muse, K. E., & St Clair, W. H. (1992). Suppression of radiation-induced neoplastic transformation by overexpression of mitochondrial superoxide dismutase. *Molecular Carcinogenesis, 6*(4), 238-242. doi:10.1002/mc.2940060404

Sterner, D. E., & Berger, S. L. (2000). Acetylation of histones and transcription-related factors. *Microbiology and molecular biology reviews : MMBR, 64*(2), 435-459. doi:10.1128/mmbr.64.2.435-459.2000

Strahl, B. D., & Allis, C. D. (2000). The language of covalent histone modifications. *Nature, 403*(6765), 41-45. doi:10.1038/47412

Svinkina, T., Gu, H., Silva, J. C., Mertins, P., Qiao, J., Fereshetian, S., . . . Carr, S. A. (2015). Deep, Quantitative Coverage of the Lysine Acetylome Using Novel Anti-acetyl-lysine Antibodies and an Optimized Proteomic Workflow. *Molecular & Cellular Proteomics, 14*(9), 2429-2440. doi:10.1074/mcp.O114.047555

Szklarczyk, D., Gable, A. L., Lyon, D., Junge, A., Wyder, S., Huerta-Cepas, J., . . . Mering, C. V. (2019). STRING v11: protein-protein association networks with increased coverage, supporting functional discovery in genome-wide experimental datasets. *Nucleic Acids Research, 47*(D1), D607-d613. doi:10.1093/nar/gky1131

Tabb, D. L., Vega-Montoto, L., Rudnick, P. A., Variyath, A. M., Ham, A.-J. L., Bunk, D. M., . . . Spiegelman, C. (2010). Repeatability and reproducibility in proteomic identifications by liquid chromatography-tandem mass spectrometry. *Journal of Proteome Research, 9*(2), 761-776. doi:10.1021/pr9006365

Tao, R., Coleman, M. C., Pennington, J. D., Ozden, O., Park, S. H., Jiang, H., . . . Gius, D. (2010). Sirt3-mediated deacetylation of evolutionarily conserved lysine 122 regulates MnSOD activity in response to stress. *Molecular Cell, 40*(6), 893-904. doi:10.1016/j.molcel.2010.12.013

Tao, Z., Gao, P., & Liu, H. W. (2009). Identification of the ADP-ribosylation sites in the PARP-1 automodification domain: Analysis and implications. *Journal of the American Chemical Society, 131*(40), 14258-14260. doi:10.1021/ja906135d

Thapa, D., Manning, J. R., Stoner, M. W., Zhang, M., Xie, B., & Scott, I. (2020). Cardiomyocyte-specific deletion of GCN5L1 in mice restricts mitochondrial protein hyperacetylation in response to a high fat diet. *Scientific Reports, 10*(1), 10665. doi:10.1038/s41598-020-67812-x

Tsai, W.-W., Wang, Z., Yiu, T. T., Akdemir, K. C., Xia, W., Winter, S., . . . Barton, M. C. (2010). TRIM24 links a non-canonical histone signature to breast cancer. *Nature, 468*(7326), 927-932. doi:10.1038/nature09542

Tyanova, S., Temu, T., Sinitcyn, P., Carlson, A., Hein, M. Y., Geiger, T., . . . Cox, J. (2016). The Perseus computational platform for comprehensive analysis of (prote)omics data. *Nature Methods, 13*, 731. doi:10.1038/nmeth.3901

Ubaida-Mohien, C., Gonzalez-Freire, M., Lyashkov, A., Moaddel, R., Chia, C. W., Simonsick, E. M., . . . Ferrucci, L. (2019). Physical Activity Associated Proteomics of Skeletal Muscle: Being Physically Active in Daily Life May Protect Skeletal Muscle From Aging. *Elife, 10*(312). doi:10.3389/fphys.2019.00312

Vassilopoulos, A., Pennington, J. D., Andresson, T., Rees, D. M., Bosley, A. D., Fearnley, I. M., . . . Gius, D. (2014). SIRT3 deacetylates ATP synthase F1 complex proteins in response to nutrient- and exercise-induced stress. *Antioxidants & redox signaling, 21*(4), 551-564. doi:10.1089/ars.2013.5420

Weinert, B. T., Iesmantavicius, V., Moustafa, T., Schölz, C., Wagner, S. A., Magnes, C., . . . Choudhary, C. (2014). Acetylation dynamics and stoichiometry in Saccharomyces cerevisiae. *Molecular Systems Biology, 10*(1), 716. doi:10.1002/msb.134766

Weinert, B. T., Moustafa, T., Iesmantavicius, V., Zechner, R., & Choudhary, C. (2015). Analysis of acetylation stoichiometry suggests that SIRT3 repairs nonenzymatic acetylation lesions. *EMBO Journal, 34*(21), 2620-2632. doi:10.15252/embj.201591271

Wen, D., Utesch, T., Wu, J., Robertson, S., Liu, J., Hu, G., & Chen, H. (2019). Effects of different protocols of high intensity interval training for VO2max improvements in adults: A meta-analysis of randomised controlled trials. *Journal of Science and Medicine in Sport, 22*(8), 941-947. doi:https://doi.org/10.1016/j.jsams.2019.01.013

Williams, A. S., Koves, T. R., Davidson, M. T., Crown, S. B., Fisher-Wellman, K. H., Torres, M. J., . . . Muoio, D. M. (2020). Disruption of acetyl-lysine turnover in muscle mitochondria promotes insulin resistance and redox stress without overt respiratory dysfunction. *Cell Metabolism, 31*(1), 131-147.e111. doi:https://doi.org/10.1016/j.cmet.2019.11.003

Wisniewski, J. R. (2017). Label-Free and Standard-Free Absolute Quantitative Proteomics Using the "Total Protein" and "Proteomic Ruler" Approaches. *Methods in Enzymology, 585*, 49-60. doi:10.1016/bs.mie.2016.10.002

Wooldridge, A. A., Fortner, C. N., Lontay, B., Akimoto, T., Neppl, R. L., Facemire, C., . . . Haystead, T. A. J. (2008). Deletion of the protein kinase A/protein kinase G target SMTNL1 promotes an exercise-adapted phenotype in vascular smooth muscle. *The Journal of Biological Chemistry, 283*(17), 11850-11859. doi:10.1074/jbc.M708628200

1235 Xiao, Y., Hsiao, T. H., Suresh, U., Chen, H. I., Wu, X., Wolf, S. E., & Chen, Y. (2014). A novel
1236 significance score for gene selection and ranking. *Bioinformatics, 30*(6), 801-807.
1237 doi:10.1093/bioinformatics/btr671

1238

1239

1240 **Appendix 1 – Key Resource Table**

Reagent type or resource	Designation	Source or reference	Identifiers	Additional information
Antibody	MYLK2 Antibody	Invitrogen	Cat#PA5-29324 RRID: AB_2546800	
Antibody	Total OXPHOS Human WB Antibody Cocktail	Abcam	Cat#ab110411 RRID: AB_2756818	
Antibody	Sirt1(Sir2) Antibody	Millipore Sigma	Cat#07-131 RRID: AB_10067921	
Antibody	Sirt3 (D22A3) Antibody	Cell Signaling Technologies	Cat#5490 RRID: AB_10828246	
Antibody	Sirt5 Antibody	Cell Signaling Technologies	Cat#8782 RRID: AB_2716763	
Antibody	Sirt6 Antibody	Cell Signaling Technologies	Cat#12486 RRID: AB_2636969	
Antibody	Acetyl-lysine Antibody	Cell Signaling Technologies	Cat#9441 RRID: AB_331805	
Antibody	P300 Mouse Antibody	Santa Cruz Biotechnologies	Cat#sc48343 RRID: AB_628075	
Antibody	Ac-H2B K20 Antibody	Abcam	Cat#ab177430	
Antibody	H2B Antibody	Cell Signaling Technologies	Cat#12364 RRID: AB_2714167	

Antibody	Ac-H3 K23 Antibody	Cell Signaling Technologies	Cat#14932 RRID: AB_2798650	
Antibody	H3 Antibody	Cell Signaling Technologies	Cat#4499 RRID: AB_10544537	
Antibody	Goat Anti-Rabbit Ig, Human ads-HRP	Southern Biotech	Cat#4010-05 RRID: AB_2632593	
Antibody	Goat Anti-Mouse	Dako (Agilent)	Cat# P0447 RRID: AB_2617137	
Biological sample	Human skeletal muscle (*vastus lateralis)*			
Cell line	C2C12 (ATCC® CRL-1772™)	ATCC	Cat#1722	
Chemical compound, drug	Glycerol	Millipore Sigma	Cat# G5516; CAS# 56-81-5	
Chemical compound, drug	Sodium pyrophosphate decahydrate	Millipore Sigma	Cat# 221368; CAS# 13472-36-1	
Chemical compound, drug	Sodium chloride	Millipore Sigma	Cat# S9888; CAS# 7647-14-5	
Chemical compound, drug	HEPES	Millipore Sigma	Cat# H3375; CAS# 7365-45-9	
Chemical compound, drug	IGEPAL CA-630, NP-40	Millipore Sigma	Cat# I8896; CAS# 9002-93-1	

Chemical compound, drug	β-Glycerophosphate disodium salt hydrate	Millipore Sigma	Cat# G9422; CAS# 154804-51-0	
Chemical compound, drug	Sodium orthovanadate	Millipore Sigma	Cat# S6508; CAS# 13721-39-6	
Chemical compound, drug	Sodium fluoride	Millipore Sigma	Cat# S1504; CAS# 7681-49-4	
Chemical compound, drug	Phenylmethanesulfonyl fluoride	Millipore Sigma	Cat# P7626; CAS# 329-98-6	
Chemical compound, drug	EDTA (for electrophoresis)	Millipore Sigma	Cat# E5134; CAS# 6381-92-6	
Chemical compound, drug	EGTA	Millipore Sigma	Cat# E4378; CAS# 67-42-5	
Chemical compound, drug	Aprotinin from bovine lung	Millipore Sigma	Cat# A1153; CAS# 9087-70-1	
Chemical compound, drug	Leupeptin	Millipore Sigma	Cat# L2884; CAS# 103476-89-7	
Chemical compound, drug	Benzamidine hydrochloride hydrate	Millipore Sigma	Cat# B6506; CAS# 206752-36-5	

Chemical compound, drug	Bovine serum albumin	Millipore Sigma	Cat# A7906; CAS# 9048-46-8	
Chemical compound, drug	Trizma base	Millipore Sigma	Cat# T1503; CAS# 77-86-1	
Chemical compound, drug	DL-Dithiothreitol	Millipore Sigma	Cat# D0632 and 43819; CAS# 3483-12-3	
Chemical compound, drug	Sodium dodecyl sulfate	Millipore Sigma	Cat# L3771; CAS# 151-21-3	
Chemical compound, drug	Bromophenol Blue sodium salt	Millipore Sigma	Cat# B8026; CAS# 34725-61-6	
Chemical compound, drug	Tween 20	Millipore Sigma	Cat# P9416; CAS# 9005-64-5	
Chemical compound, drug	Skimmed milk powder	Easis	Cat# 801300	
Chemical compound, drug	Glycine	Millipore Sigma	Cat# G7126; CAS# 56-40-6	
Chemical compound, drug	2-propanol	Millipore Sigma	Cat# 109634; CAS# 67-63-0	

Chemical compound, drug	Ethanol 96%	Plum	Cat# 201146; CAS# 64-17-5	
Chemical compound, drug	Brilliant Blue R	Millipore Sigma	Cat# B7920; CAS# 6104-59-2	
Chemical compound, drug	Acetic acid (glacial) 100%	Millipore Sigma	Cat# 100063; CAS# 64-19-7	
Chemical compound, drug	Precision plus all blue	BioRad	Cat# 1610373	
Chemical compound, drug	Precision plus dual color	BioRad	Cat# 1610374	
Chemical compound, drug	Immobilon Forte Western HRP substrate	Millipore Sigma	Cat# WBLUF 0500	
Chemical compound, drug	Bovine Serum Albumin Standard	Thermo Fisher Scientific	Cat# 23209	
Chemical compound, drug	BCA Protein Assay Reagent A	Thermo Fisher Scientific	Cat# 23223	
Chemical compound, drug	BCA Protein Assay Reagent B	Thermo Fisher Scientific	Cat# 23224	

Chemical compound, drug	Potassium phosphate dibasic trihydrate	Millipore Sigma	Cat# P9666; CAS# 16788-57-1	
Chemical compound, drug	Potassium dihydrogen phosphate	Millipore Sigma	Cat# 1.04873; CAS# 7778-77-0	
Chemical compound, drug	BCA Protein Assay Kit	Thermo Fisher Scientific	Cat# 23225	
Chemical compound, drug	Trizma hydrochloride	Millipore Sigma	Cat# T3253; CAS# 1185-53-1	
Chemical compound, drug	EDTA	Millipore Sigma	Cat# E9884; CAS# 60-00-4	
Chemical compound, drug	NAD	Millipore Sigma	Cat# NAD100-RO; CAS# 53-84-9	
Chemical compound, drug	L-(−)-Malic acid sodium salt	Millipore Sigma	Cat# M1125; CAS# 68303-40-2	
Chemical compound, drug	Acetyl-Coenzyme A	Millipore Sigma	Cat# ACOA-RO	
Chemical compound, drug	L-Malate Dehydrogenase (L-MDH)	Millipore Sigma	Cat# LMDH-RO	

Chemical compound, drug	NADH	Millipore Sigma	Cat# 10107735001	
Chemical compound, drug	Sucrose	Millipore Sigma	Cat# S7903; CAS# 57-50-1	
Chemical compound, drug	Magnesium chloride hexahydrate	Millipore Sigma	Cat# M2670; CAS# 7791-18-6	
Chemical compound, drug	Taurine	Millipore Sigma	Cat# T0625; CAS# 107-35-7	
Chemical compound, drug	Potassium Dihydrogen Phosphate	Millipore Sigma	Cat# P9791; CAS# 7778-77-0	
Chemical compound, drug	HEPES	Millipore Sigma	Cat# H3375; CAS# 7365-45-9	
Chemical compound, drug	Bovine serum albumin (fatty acid free)	Millipore Sigma	Cat# A7030; CAS# 9048-46-8	
Chemical compound, drug	Catalase from bovine liver	Millipore Sigma	Cat# C9322; CAS# 9001-05-2	
Chemical compound, drug	Lactobionic acid	Millipore Sigma	Cat# 153516; CAS# 96-82-2	

Chemical compound, drug	MES potassium salt	Millipore Sigma	Cat# M0895; CAS# 39946-25-3	
Chemical compound, drug	ATP	Millipore Sigma	Cat# A3377; CAS# 34369-07-8	
Chemical compound, drug	Sodium creatine phosphate dibasic tetrahydrate	Millipore Sigma	Cat# 27920; CAS# 71519-72-7	
Chemical compound, drug	Imidazole	Millipore Sigma	Cat# I0250; CAS# 288-32-4	
Chemical compound, drug	Potassium hydroxide	Millipore Sigma	Cat# P1767; CAS# 1310-58-3	
Chemical compound, drug	Calcium carbonate	Millipore Sigma	Cat# C4830; CAS# 471-34-1	
Chemical compound, drug	Saponin from quillaja bark	Millipore Sigma	Cat# S7900; CAS# 8047-15-2	
Chemical compound, drug	L-(−)-Malic acid sodium salt	Millipore Sigma	Cat# M1125; CAS# 68303-40-2	
Chemical compound, drug	Octanoyl-L-carnitine	Millipore Sigma	Cat# 50892; CAS# 25243-95-2	

Chemical compound, drug	ADP	Millipore Sigma	Cat# A5285; CAS# 72696-48-1	
Chemical compound, drug	L-glutamic acid monosodium salt monohydrate	Millipore Sigma	Cat# 49621; CAS# 6106-04-3	
Chemical compound, drug	Sodium succinate dibasic hexahydrate	Millipore Sigma	Cat# S2378; CAS# 6106-21-4	
Chemical compound, drug	Cytochrome c from equine heart	Millipore Sigma	Cat# C2506; CAS# 9007-43-6	
Chemical compound, drug	FCCP	Millipore Sigma	Cat# C2920; CAS# 370-86-5	
Chemical compound, drug	Rotenone	Millipore Sigma	Cat# R8875; CAS# 83-79-4	
Chemical compound, drug	Malonic acid	Millipore Sigma	Cat# M1296; CAS# 141-82-2	
Chemical compound, drug	Myxothiazol	Millipore Sigma	Cat# T5580; CAS# 76706-55-3	
Chemical compound, drug	Antimycin A from Streptomyces sp.	Millipore Sigma	Cat# A8674; CAS# 1397-94-0	

Chemical compound, drug	Sodium deoxycholate	Sigma-Aldrich	Cat# D6750 CAS# 302-95-4	
Chemical compound, drug	Tris(2-carboxyethyl)phosphine hydrochloride	Sigma-Aldrich	Cat# C4706 CAS# 51805-45-9	
Chemical compound, drug	2-Chloroacetamide	Sigma-Aldrich	Cat# 22790 CAS# 79-07-2	
Chemical compound, drug	Trypsin	Sigma-Aldrich	Cat# T7575	
Chemical compound, drug	Lysine	Wako	Cat# 124-06871	
Chemical compound, drug	DMEM high glucose	Gibco	Cat# 41965039	
Chemical compound, drug	Fetal bovine serum(FBS)	Sigma-Aldrich	Cat# F7524	
Chemical compound, drug	Penicillin-Streptomycin, liquid	Gibco	Cat# 15070-063	
Chemical compound, drug	Opti-MEM™ I Reduced Serum Medium	Gibco	Cat# 31985062	

Chemical compound, drug	TransIT-X2 Dynamic Delivery System	Mirus Bio	Cat# MIR6003	
Sequence-based reagent	EP300 siRNA	Merck Sigma	Cat# SASI_Mm01_00159721	
Commercial assay, kit	PTMScan® Acetyl-Lysine Motif [Ac-K] Kit	Cell Signaling Technologies	Cat#13416	
Software, algorithm,	Graphpad Prism 8.0	https://www.graphpad.com/	RRID: SCR_002798	
Software, algorithm	MaxQuant 1.5.3.30	https://maxquant.org/	RRID: SCR_014485	
Software, algorithm	Spectronaut v14	https://biognosys.com/shop/spectronaut		
Software, algorithm	Perseus 1.6.10.50	http://www.coxdocs.org/doku.php?id=perseus:start	RRID: SCR_015753	
Software, algorithm	R Studio	https://rstudio.com/	RRID: SCR_000432	
Software, algorithm	Cytoscape v3.7.2	www.cytoscape.org	RRID: SCR_003032	
Software, algorithm	iceLogo	https://iomics.ugent.be/icelogoserver/	RRID: SCR_012137	

Software, algorithm	Adobe Illustrator 24.3	https://www.adobe.com/products/illustrator	RRID: SCR_010279	
Software, algorithm	Bio-Rad Image Studio	https://www.licor.com/bio/products/Software,algorithm/image_studio/	RRID: SCR_014210	
Software, algorithm	Oroboros DatLab 6 V. 6.1.0.7	https://www.oroboros.at/index.php/product/datlab/		
Other	10% Criterion TGX Stain-Free gel	BioRad	Cat# 567-8035	
Other	16.5% Criterion Tris-Tricine/Peptide gel	BioRad	Cat# 345-0065	
Other	Immobilon-P PVDF membrane	Millipore Sigma	Cat# IPVH00010	
Other	Whatman cellulose chromatography papers	Millipore Sigma	Cat# WHA3030917	
Other	Stainless Steel Beads 5mm	Qiagen	Cat# 69989	
Other	Stuart Rotator Drive STR4	Stuart-equipment	Cat# STR4	
Other	Hettich universal 320 R centrifuge	Andrea Hettich GmbH, Germany	Cat# 1406	
Other	E_{max} precision microplate reader	Molecular Devices	Cat# LR88026	
Other	PowerPac HC Power Supply	BioRad	Cat# 1645052	

Other	TE 77 ECL Semi-Dry Transfer Unit	Amersham Biosciences	Cat# 80-6211-86	
Other	ChemiDoc MP Imaging System	BioRad	Cat# 731BR00119	
Other	White 96-Well Immuno Plates	Fischer Scientific	Cat# 10415985	
Other	Fluoroskan, Microplate Fluorometer, one dispenser	Fischer Scientific	Cat# 5200111	
Other	Non-treated 96-Well Microplates	Fischer Scientific	Cat# 10252711	
Other	Multiskan FC Microplate Photometer	Fischer Scientific	Cat# 11500695	
Other	Sep-Pak C18 Cartrige	Waters	Cat# WAT054955	

Figure 1

A

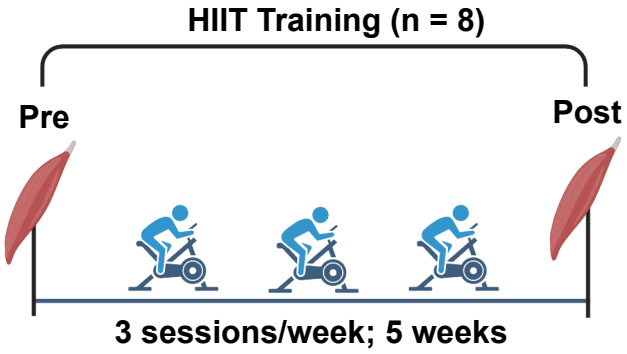

B

Subject characteristics

	Pre	Post
Age (years)	27 ± 2	
Height (cm)	187 ± 2	
Weight (kg)	82.2 ± 3.7	81.8 ± 3.4
BMI (kg·m^{-2})	23.5 ± 0.9	23.4 ± 0.8
Lean mass (kg)	59.1 ± 1.2	60.1 ± 1.2**
Fat mass (kg)	19.7 ± 2.9	18.9 ± 2.6
$\dot{V}O_2$max (mL·min^{-1})	3669 ± 334	4200 ± 117***
$\dot{V}O_2$max (mL·kg^{-1}·min^{-1})	45.3 ± 6.9	51.8 ± 1.9***
iPPO (W)	340 ± 18	400 ± 13***

C

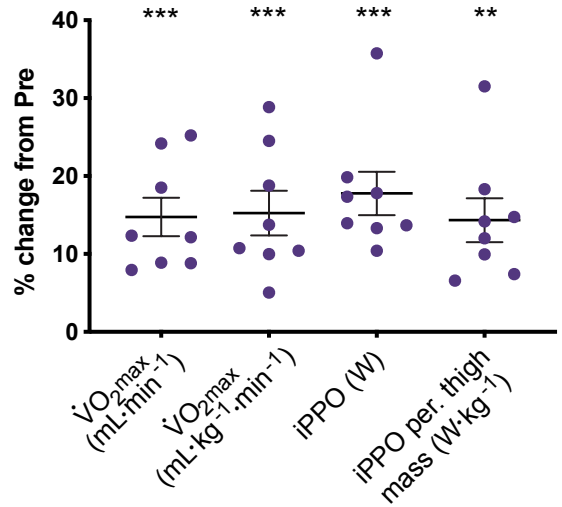

D

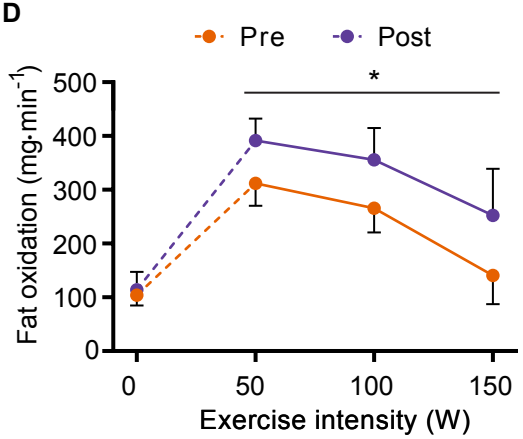

E

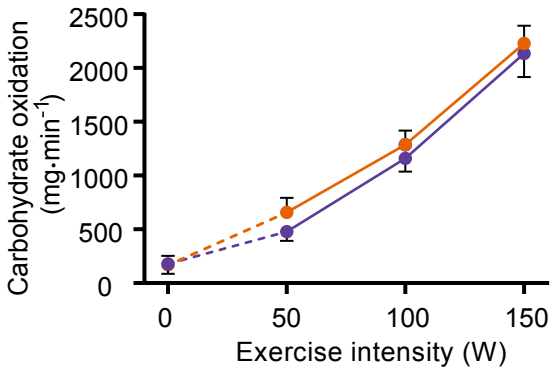

F

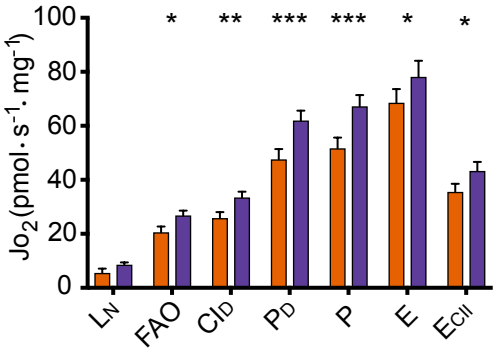

G

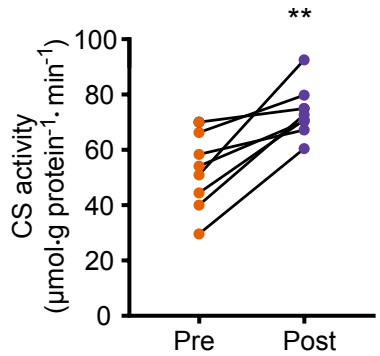

H

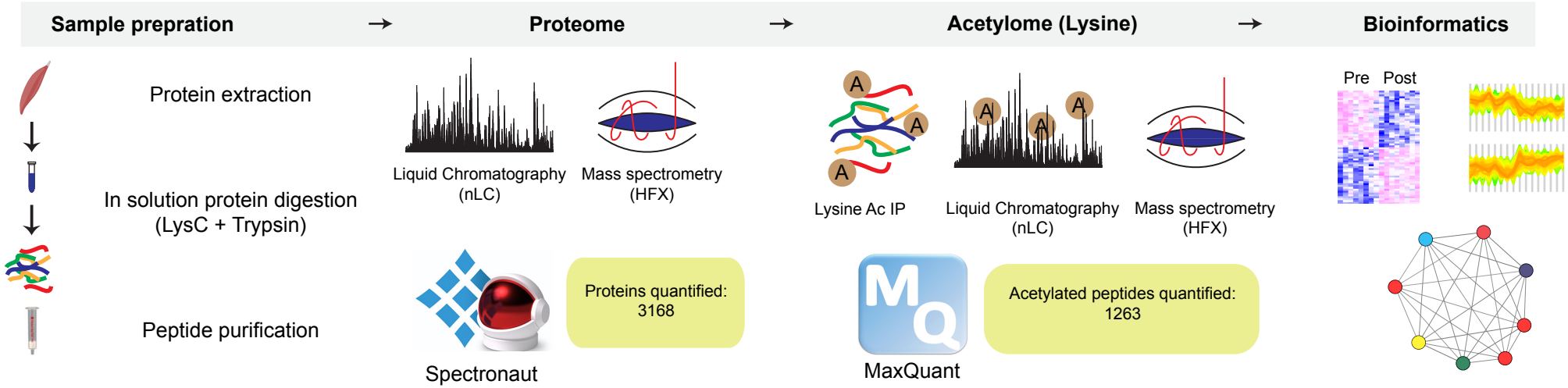

Figure 2

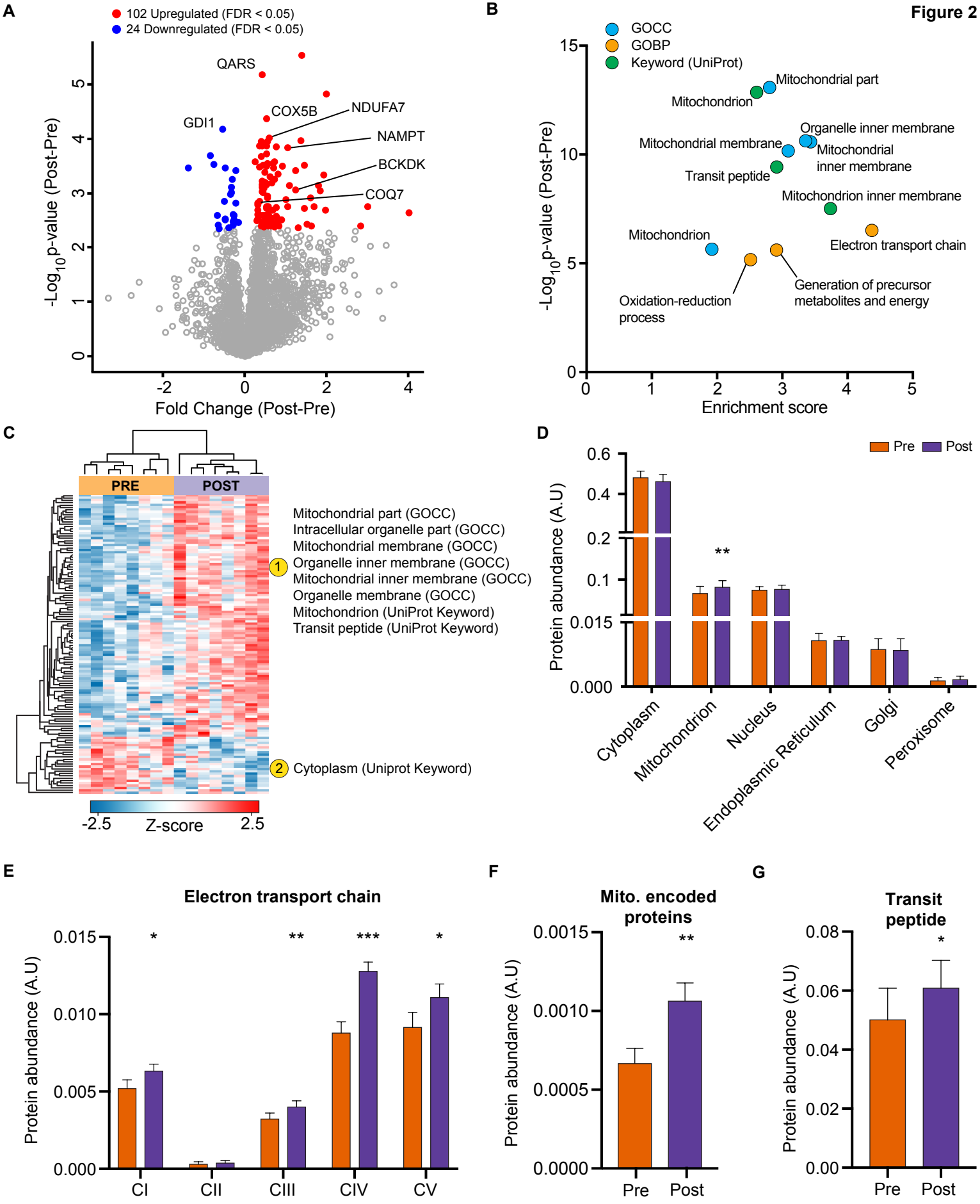
A
102 Upregulated (FDR < 0.05)
24 Downregulated (FDR < 0.05)
QARS
COX5B
NDUFA7
GDI1
NAMPT
BCKDK
COQ7
-Log10 p-value (Post-Pre)
Fold Change (Post-Pre)
B
GOCC
GOBP
Keyword (UniProt)
Mitochondrial part
Mitochondrion
Organelle inner membrane
Mitochondrial membrane
Mitochondrial inner membrane
Transit peptide
Mitochondrion inner membrane
Electron transport chain
Mitochondrion
Generation of precursor metabolites and energy
Oxidation-reduction process
-Log10 p-value (Post-Pre)
Enrichment score
C
PRE
POST
Mitochondrial part (GOCC)
Intracellular organelle part (GOCC)
Mitochondrial membrane (GOCC)
1 Organelle inner membrane (GOCC)
Mitochondrial inner membrane (GOCC)
Organelle membrane (GOCC)
Mitochondrion (UniProt Keyword)
Transit peptide (UniProt Keyword)
2 Cytoplasm (Uniprot Keyword)
-2.5
Z-score
2.5
D
Pre
Post
Protein abundance (A.U)
Cytoplasm
Mitochondrion
Nucleus
Endoplasmic Reticulum
Golgi
Peroxisome
E
Electron transport chain
Protein abundance (A.U)
CI
CII
CIII
CIV
CV
F
Mito. encoded proteins
Protein abundance (A.U)
Pre
Post
G
Transit peptide
Protein abundance (A.U)
Pre
Post

Figure 3

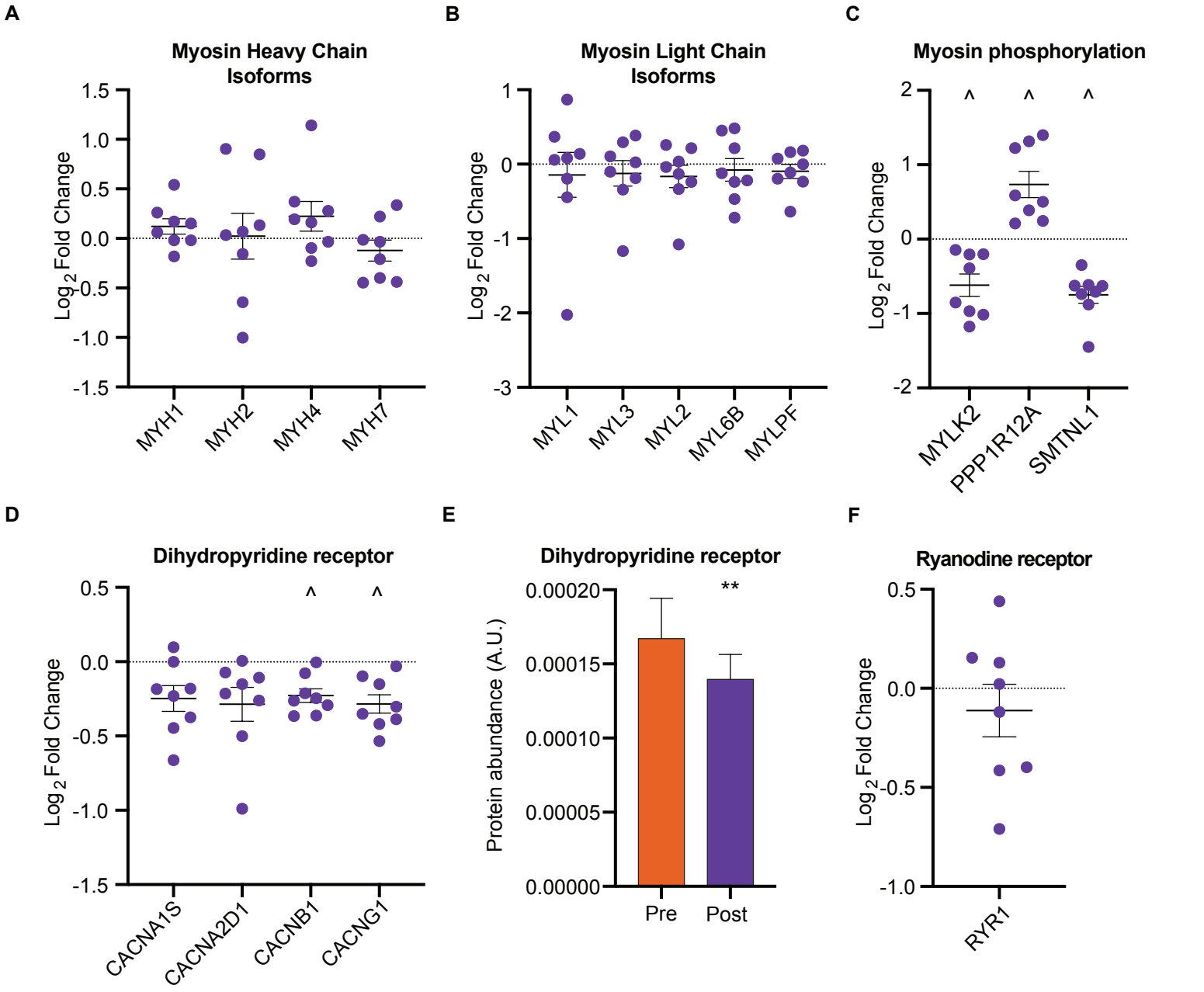
A
Myosin Heavy Chain Isoforms
Log2 Fold Change
1.5
1.0
0.5
0.0
-0.5
-1.0
-1.5
MYH1
MYH2
MYH4
MYH7
B
Myosin Light Chain Isoforms
Log2 Fold Change
1
0
-1
-2
-3
MYL1
MYL3
MYL2
MYL6B
MYLPF
C
Myosin phosphorylation
Log2 Fold Change
2
1
0
-1
-2
^
^
^
MYLK2
PPP1R12A
SMTNL1
D
Dihydropyridine receptor
Log2 Fold Change
0.5
0.0
-0.5
-1.0
-1.5
^
^
CACNA1S
CACNA2D1
CACNB1
CACNG1
E
Dihydropyridine receptor
Protein abundance (A.U.)
0.00020
0.00015
0.00010
0.00005
0.00000
**
Pre
Post
F
Ryanodine receptor
Log2 Fold Change
0.5
0.0
-0.5
-1.0
RYR1

Figure 4

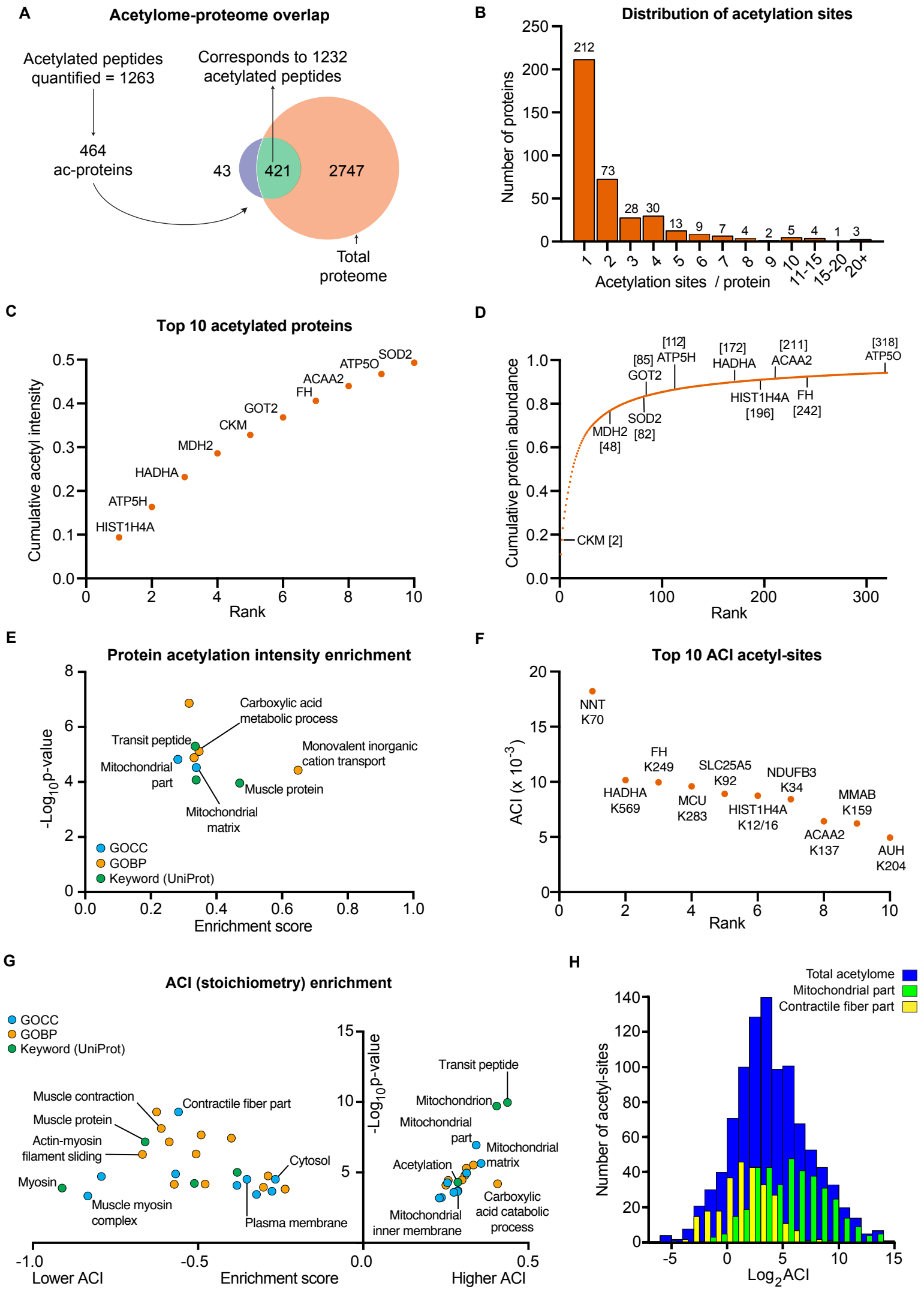
A
Acetylome-proteome overlap
Acetylated peptides quantified = 1263
464 ac-proteins
Corresponds to 1232 acetylated peptides
43
421
2747
Total proteome
B
Distribution of acetylation sites
Number of proteins
Acetylation sites / protein
212
73
28
30
13
9
7
4
2
5
4
1
3
1
2
3
4
5
6
7
8
9
10
11-15
15-20
20+
C
Top 10 acetylated proteins
Cumulative acetyl intensity
Rank
SOD2
ATP5O
ACAA2
FH
GOT2
CKM
MDH2
HADHA
ATP5H
HIST1H4A
D
Cumulative protein abundance
Rank
[318] ATP5O
[211] ACAA2
[172] HADHA
[112] ATP5H
[85] GOT2
HIST1H4A [196]
FH [242]
SOD2 [82]
MDH2 [48]
CKM [2]
E
Protein acetylation intensity enrichment
-Log10p-value
Enrichment score
Carboxylic acid metabolic process
Transit peptide
Monovalent inorganic cation transport
Mitochondrial part
Muscle protein
Mitochondrial matrix
GOCC
GOBP
Keyword (UniProt)
F
Top 10 ACI acetyl-sites
ACI (x 10-3)
Rank
NNT K70
FH K249
SLC25A5 K92
NDUFB3 K34
HADHA K569
MCU K283
HIST1H4A K12/16
MMAB K159
ACAA2 K137
AUH K204
G
ACI (stoichiometry) enrichment
GOCC
GOBP
Keyword (UniProt)
-Log10p-value
Muscle contraction
Contractile fiber part
Muscle protein
Actin-myosin filament sliding
Myosin
Muscle myosin complex
Cytosol
Plasma membrane
Transit peptide
Mitochondrion
Mitochondrial part
Mitochondrial matrix
Acetylation
Carboxylic acid catabolic process
Mitochondrial inner membrane
Lower ACI
Enrichment score
Higher ACI
H
Total acetylome
Mitochondrial part
Contractile fiber part
Number of acetyl-sites
Log2ACI

Figure 5

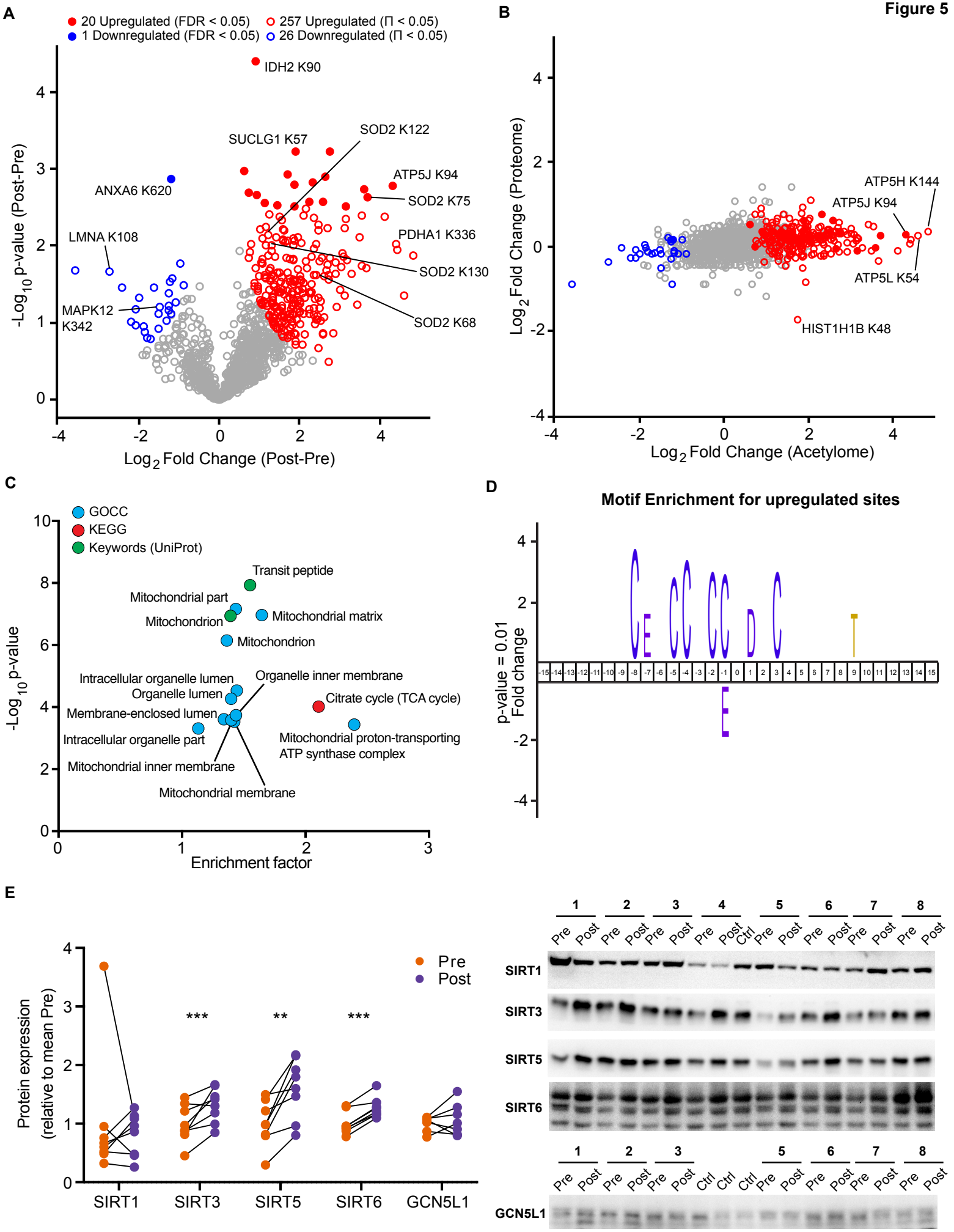
A
20 Upregulated (FDR < 0.05)
257 Upregulated (Π < 0.05)
1 Downregulated (FDR < 0.05)
26 Downregulated (Π < 0.05)
IDH2 K90
SUCLG1 K57
SOD2 K122
ATP5J K94
SOD2 K75
ANXA6 K620
PDHA1 K336
LMNA K108
SOD2 K130
MAPK12 K342
SOD2 K68
-Log10 p-value (Post-Pre)
Log2 Fold Change (Post-Pre)
B
ATP5H K144
ATP5J K94
ATP5L K54
HIST1H1B K48
Log2 Fold Change (Proteome)
Log2 Fold Change (Acetylome)
C
GOCC
KEGG
Keywords (UniProt)
Transit peptide
Mitochondrial part
Mitochondrion
Mitochondrial matrix
Mitochondrion
Intracellular organelle lumen
Organelle inner membrane
Organelle lumen
Citrate cycle (TCA cycle)
Membrane-enclosed lumen
Intracellular organelle part
Mitochondrial proton-transporting ATP synthase complex
Mitochondrial inner membrane
Mitochondrial membrane
-Log10 p-value
Enrichment factor
D
Motif Enrichment for upregulated sites
p-value = 0.01
Fold change
E
Pre
Post
***
**
***
Protein expression (relative to mean Pre)
SIRT1
SIRT3
SIRT5
SIRT6
GCN5L1
Ctrl

Figure 6

A

Protein:

Log$_2$ fold change (protein)

-2 2

Undetected

Acetylation site:

- Upregulated (Π < 0.05)
- Downregulated (Π < 0.05)
- Unchanged (Π > 0.05)

NDUFAB1, NDUFA9, NDUFA10, NDUFV1, NDUFA2, NDUFV2, NDUFB9, NDUFV3, NDUFA7, NDUFB6, NDUFS5, NDUFS6, NDUFS1, NDUFA5, NDUFB3

SDHA, SDHB

MT-ATP8, ATP5H, ATP5B, ATP5O, ATP5C1, ATP5J, ATP5D, ATP5L, ATP5F1, ATP5A1, ATPIF1, ATP5E

CI, CII, CIII, CIV, CV

UQCRC2, CYC1, UQCRB, UQCRH, UQCRC1

COX4I1, COX6B1, COX5B

B

Pyruvate

PDHX, PDHA1, DLAT

Acetyl CoA

CS

Oxaloacetate

Citrate

ACO2

MDH1, MDH2

Malate

Isocitrate

IDH3A, IDH1, IDH3B, IDH2

FH

TCA Cycle

Fumarate

2-oxogluterate

SDHA, SDHB

OGDH, DLST

Succinate

SUCLG2, SUCLG1, DLD

Succinyl CoA

SUCLA2

C

ACTC1, MYH4, MYBPC1, ACTN2

MYL1, MYH3, MYL2, TNNT1, TNNI1

MYH7, MYH9, TPM2, NEB

ACTN3, DMD, MYH1, TTN

TPM4

VIM

TNNT3, TNNI2, MYL3, DES

MYH2, TPM1, TPM3, MYBPC2

Figure 7

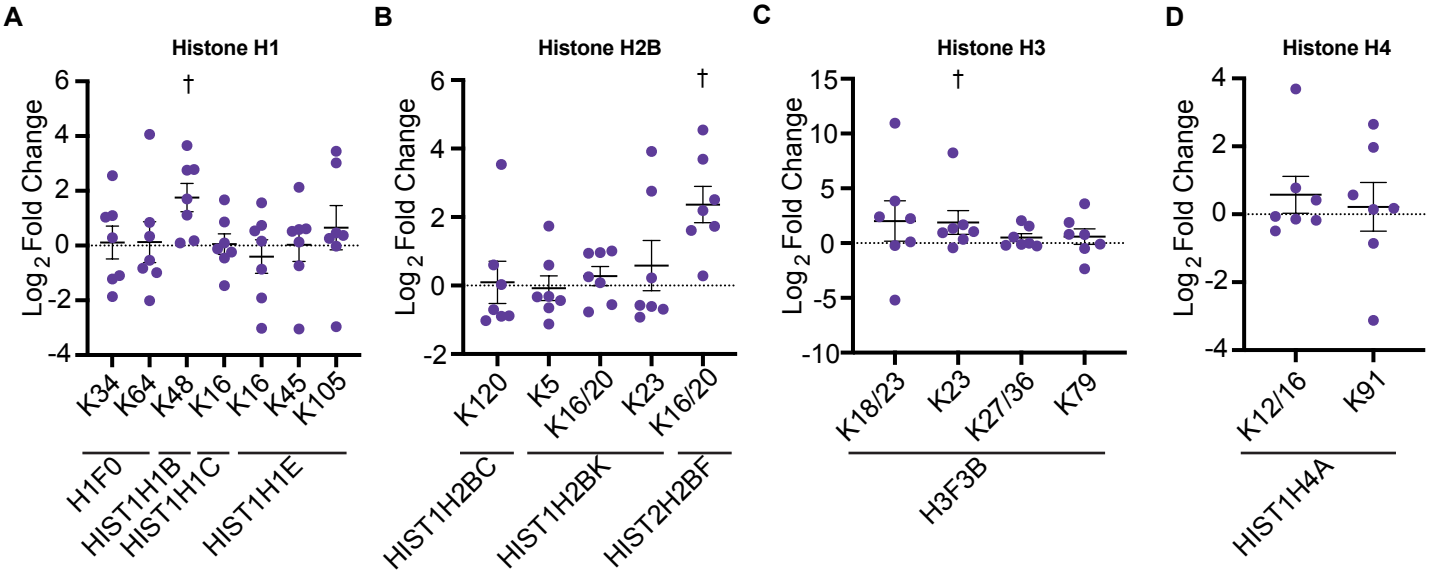
A
Histone H1
Log2 Fold Change
6
4
2
0
-2
-4
†
K34
K64
K48
K16
K16
K45
K105
H1F0
HIST1H1B
HIST1H1C
HIST1H1E
B
Histone H2B
Log2 Fold Change
6
4
2
0
-2
†
K120
K5
K16/20
K23
K16/20
HIST1H2BC
HIST1H2BK
HIST2H2BF
C
Histone H3
Log2 Fold Change
15
10
5
0
-5
-10
†
K18/23
K23
K27/36
K79
H3F3B
D
Histone H4
Log2 Fold Change
4
2
0
-2
-4
K12/16
K91
HIST1H4A

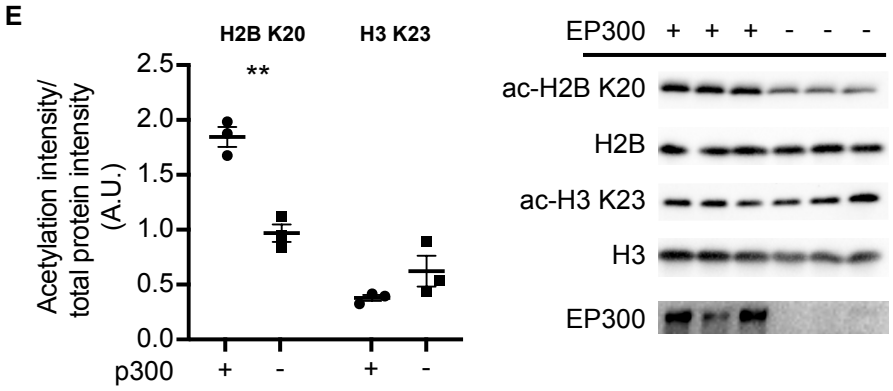
E
H2B K20
H3 K23
Acetylation intensity/
total protein intensity
(A.U.)
2.5
2.0
1.5
1.0
0.5
0.0
**
p300
+
-
+
-
EP300 + + + - - -
ac-H2B K20
H2B
ac-H3 K23
H3
EP300

Figure S1

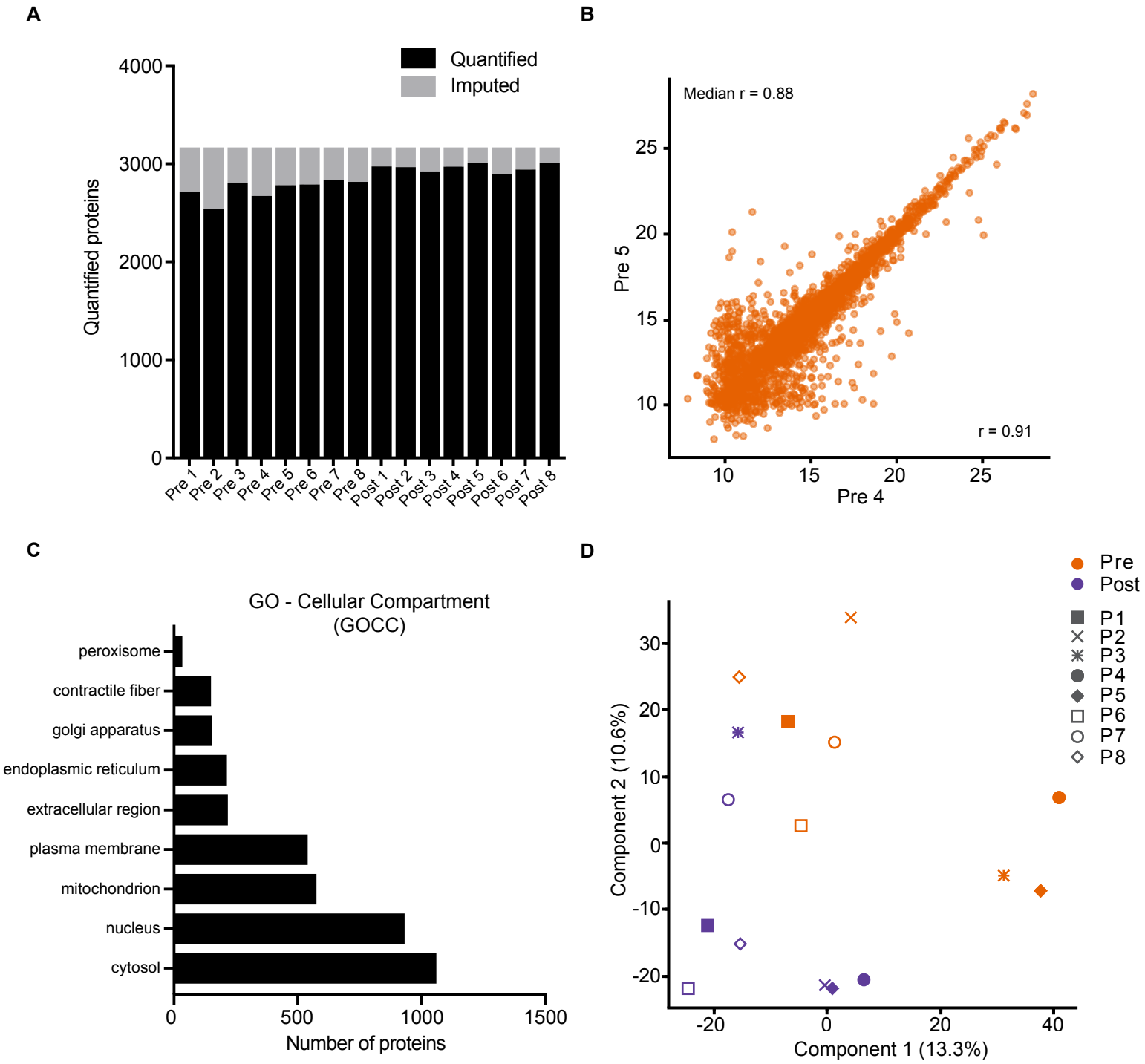
A
Quantified
Imputed
Quantified proteins
4000
3000
2000
1000
0
Pre 1
Pre 2
Pre 3
Pre 4
Pre 5
Pre 6
Pre 7
Pre 8
Post 1
Post 2
Post 3
Post 4
Post 5
Post 6
Post 7
Post 8
B
Median r = 0.88
r = 0.91
Pre 5
Pre 4
10
15
20
25
C
GO - Cellular Compartment
(GOCC)
peroxisome
contractile fiber
golgi apparatus
endoplasmic reticulum
extracellular region
plasma membrane
mitochondrion
nucleus
cytosol
0
500
1000
1500
Number of proteins
D
Pre
Post
P1
P2
P3
P4
P5
P6
P7
P8
Component 2 (10.6%)
Component 1 (13.3%)
30
20
10
0
-10
-20
40

Figure S2

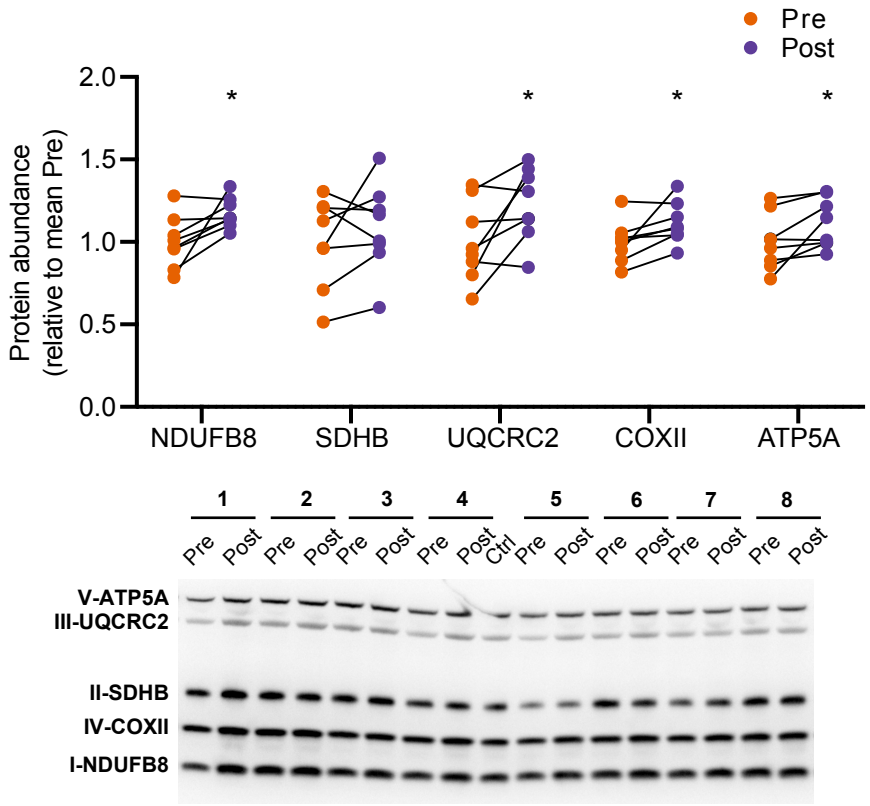
Pre
Post
Protein abundance
(relative to mean Pre)
2.0
1.5
1.0
0.5
0.0
*
*
*
*
NDUFB8
SDHB
UQCRC2
COXII
ATP5A
1
2
3
4
5
6
7
8
Pre
Post
Pre
Post
Pre
Post
Pre
Post
Ctrl
Pre
Post
Pre
Post
Pre
Post
Pre
Post
V-ATP5A
III-UQCRC2
II-SDHB
IV-COXII
I-NDUFB8

Figure S3

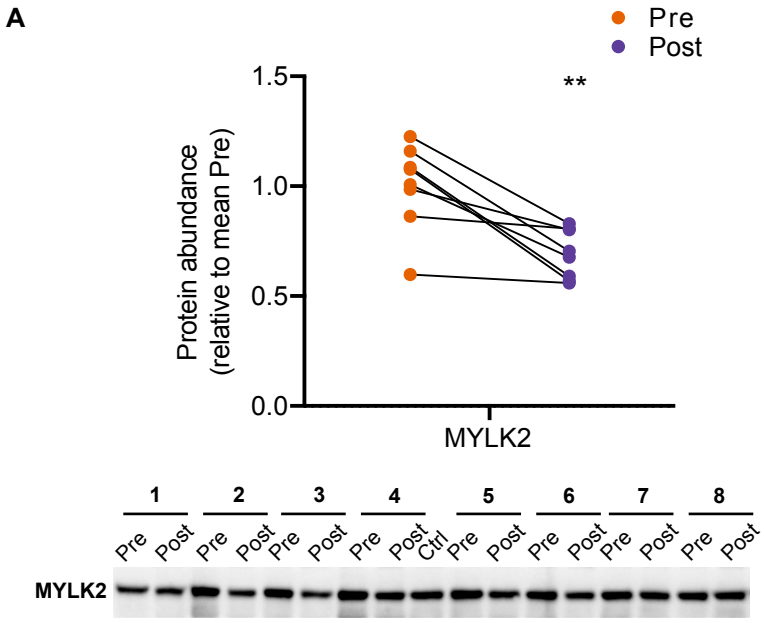
A
Pre
Post
Protein abundance
(relative to mean Pre)
1.5
1.0
0.5
0.0
**
MYLK2
1
2
3
4
5
6
7
8
Pre
Post
Ctrl
MYLK2

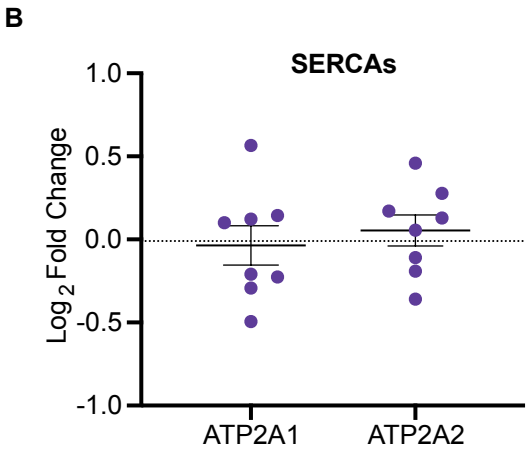
B
SERCAs
Log 2 Fold Change
1.0
0.5
0.0
-0.5
-1.0
ATP2A1
ATP2A2

Figure S4

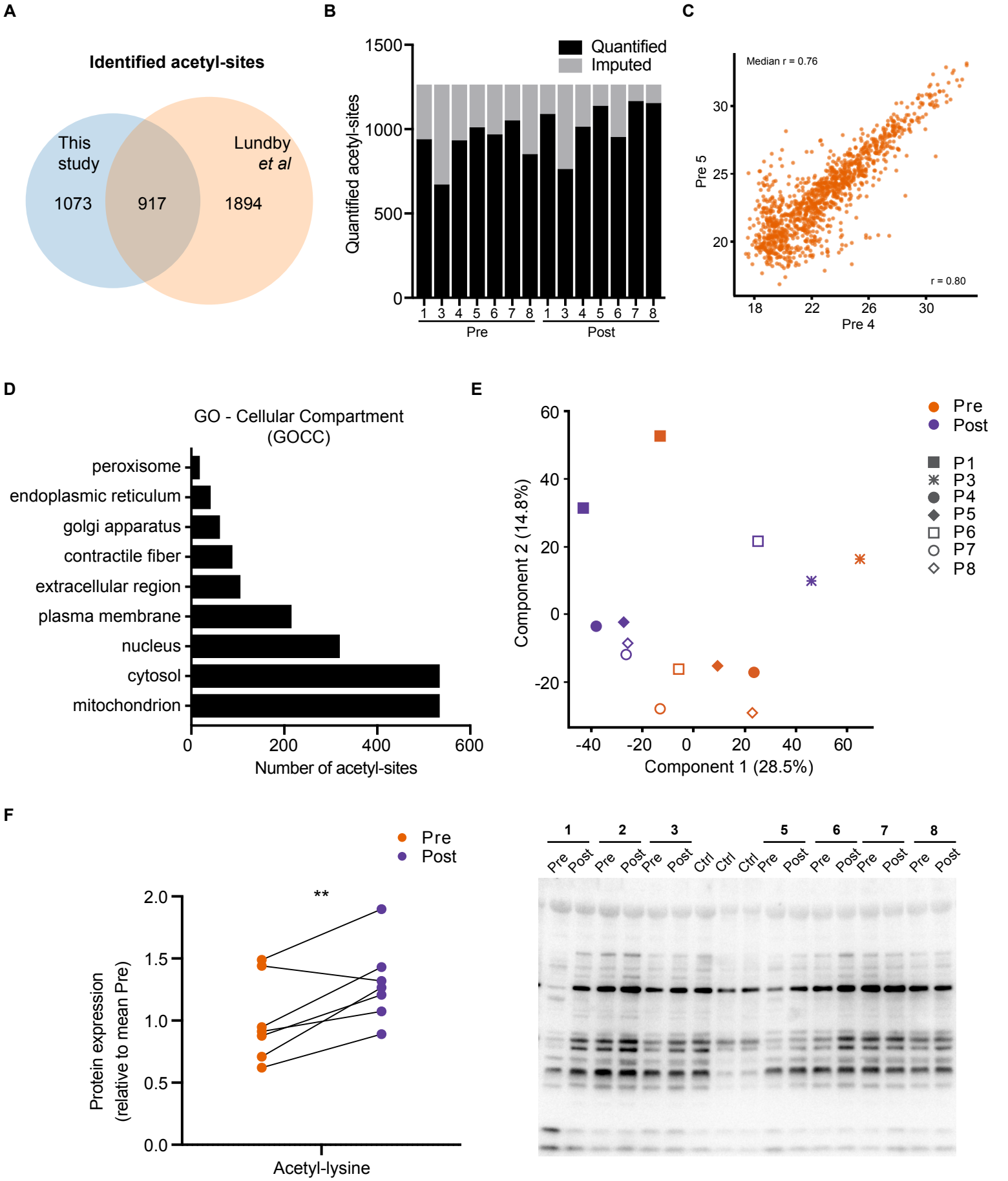
A
Identified acetyl-sites
This study
Lundby et al
1073
917
1894
B
Quantified
Imputed
Quantified acetyl-sites
1500
1000
500
0
1 3 4 5 6 7 8 1 3 4 5 6 7 8
Pre
Post
C
Median r = 0.76
r = 0.80
Pre 5
Pre 4
18 22 26 30
20 25 30
D
GO - Cellular Compartment (GOCC)
peroxisome
endoplasmic reticulum
golgi apparatus
contractile fiber
extracellular region
plasma membrane
nucleus
cytosol
mitochondrion
0 200 400 600
Number of acetyl-sites
E
Pre
Post
P1
P3
P4
P5
P6
P7
P8
Component 2 (14.8%)
Component 1 (28.5%)
60 40 20 0 -20
-40 -20 0 20 40 60
F
Pre
Post
**
Protein expression (relative to mean Pre)
2.0 1.5 1.0 0.5 0.0
Acetyl-lysine
1 2 3 5 6 7 8
Pre Post Pre Post Pre Post Ctrl Ctrl Ctrl Pre Post Pre Post Pre Post Pre Post

Figure S5

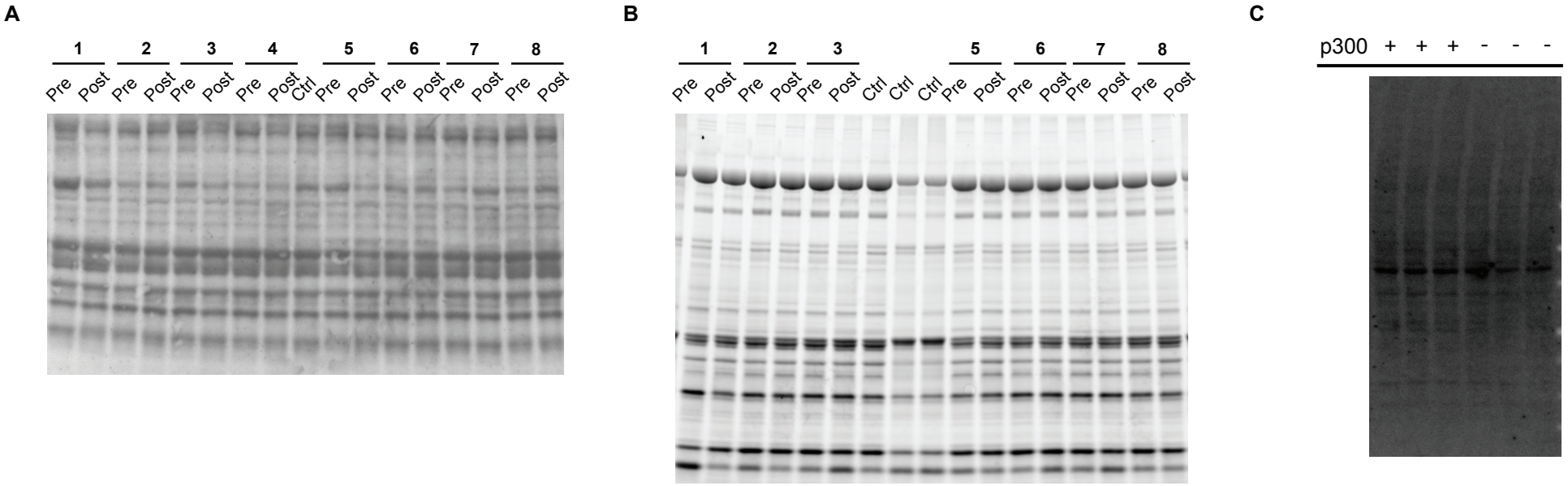
A
1
2
3
4
5
6
7
8
Pre
Post
Pre
Post
Pre
Post
Pre
Post
Ctrl
Pre
Post
Pre
Post
Pre
Post
Pre
Post
B
1
2
3
5
6
7
8
Pre
Post
Pre
Post
Pre
Post
Ctrl
Ctrl
Ctrl
Pre
Post
Pre
Post
Pre
Post
Pre
Post
C
p300 + + + - - -
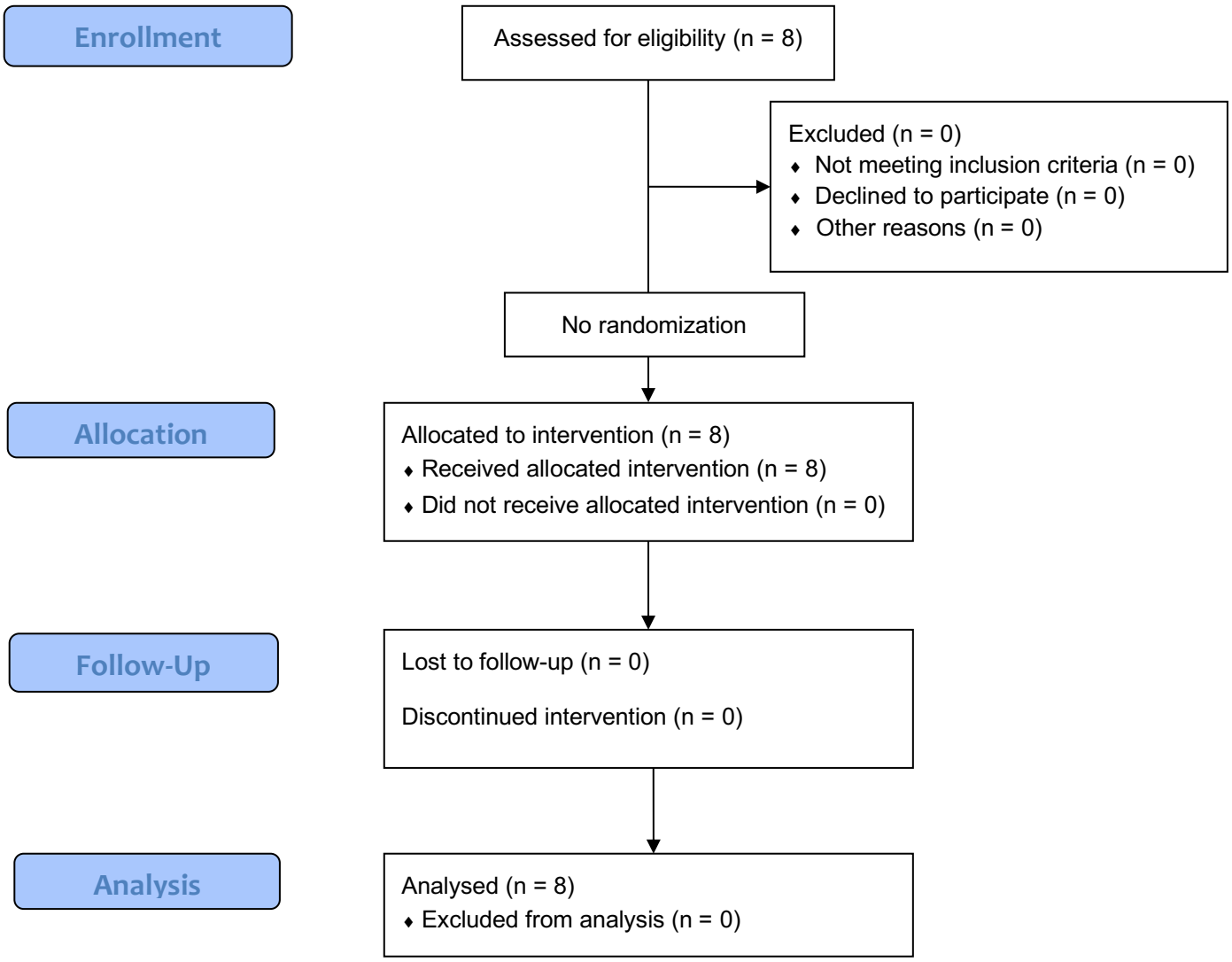
CONSORT Flow Diagram